THE ASTROPHYSICAL JOURNAL, 460:777–793, 1996 April 1

THE MAGNETOHYDRODYNAMIC KELVIN-HELMHOLTZ INSTABILITY: A TWO-DIMENSIONAL NUMERICAL STUDY

ADAM FRANK,[1] T. W. JONES,[2] DONGSU RYU,[3] AND JOSEPH B. GAALAAS[4]

Received 1995 June 12; accepted 1995 October 9

ABSTRACT

We have carried out two-dimensional simulations of the nonlinear evolution of unstable sheared magnetohydrodynamic flows. These calculations extend the earlier work of Miura (1984) and consider periodic sections of flows containing aligned magnetic fields. Two equal density, compressible fluids are separated by a shear layer with a hyperbolic tangent velocity profile. We considered two cases: a strong magnetic field (Alfvén Mach number, $M_A = 2.5$) and a weak field ($M_A = 5$). Each flow rapidly evolves until it reaches a nearly steady condition, which is fundamentally different from the analogous gasdynamic state. Both MHD flows relax to a stable, laminar flow on timescales less than or of the order of 15 linear growth times, measured from saturation of the instability. That timescale is several orders of magnitude less than the nominal dissipation time for these simulated flows, so this condition represents an quasi-steady relaxed state analogous to the long-lived single vortex, known as "Kelvin's Cat's Eye," formed in two-dimensional nearly ideal gasdynamic simulations of a vortex sheet.

The strong magnetic field case reaches saturation as magnetic tension in the displaced flow boundary becomes sufficient to stabilize it. That flow then relaxes in a straightforward way to the steady, laminar flow condition. The weak magnetic field case, on the other hand, begins development of the vortex expected for gasdynamics, but that vortex is destroyed by magnetic stresses that locally become strong. Magnetic topologies lead to reconnection and dynamical alignment between magnetic and velocity fields. Together these processes produce a sequence of intermittent vortices and subsequent relaxation to a nearly laminar flow condition in which the magnetic cross helicity is nearly maximized. Remaining irregularities show several interesting properties. A pair of magnetic flux tubes are formed that straddle the boundary between the oppositely moving fluids. Velocity and magnetic fluctuations within those features are closely aligned, representing Alfvén waves propagating locally downstream. The flux tubes surround a low-density channel of hot gas that contains most of the excess entropy generated through the relaxation process.

Subject headings: instabilities — methods: numerical — MHD — turbulence

1. INTRODUCTION

Sheared boundary flows are ubiquitous in astrophysical environments as diverse as Earth's magnetopause and supersonic jets. The susceptibility of such boundaries to the Kelvin-Helmholtz (KH) instability is well-known (see, e.g., Chandrasekhar 1961; Birkinshaw 1991). Development of the KH instability leads to momentum and energy transport, dissipation, mixing of fluids and, when magnetic fields are involved, the possibility of field amplification, reconnection and dynamical alignment, or self-organization processes. Although the nonlinear evolution of the KH instability has been studied in considerable detail for nonmagnetized fluids through extensive analytical calculations and numerical simulations (see, e.g., Corcos & Sherman 1984, and references therein), much less progress has been made in understanding the nature of the KH instability in magnetohydrodynamics (MHD). That is both because the MHD KH instability is substantially more complex and because until recently adequate numerical MHD simulations were difficult. Yet it is clear that understanding the physics of the MHD KH instability would be very useful in a wide variety of contexts.

The basic MHD KH linear stability analysis was carried out a long time ago (see, e.g., Chandrasekhar 1961), and it has since been applied to numerous astrophysical situations including those requiring cylindrical geometries (see, e.g., Ferrari, Trussoni, & Zaninetti 1981; Fiedler & Jones 1984). It is clear from these studies that the influence a magnetic field has on the stability of an initial flow equilibrium depends on both the strength and orientation of the field. Obviously, an equilibrium exists only when the field initially is parallel to the shear layer. When the field is aligned also with the flow vectors, magnetic tension directly inhibits the instability, while if the field is perpendicular, its role in ideal MHD comes through pressure contributions modifying the characteristic magnetosonic wave speed. For equal density, incompressible, inviscid fluid layers separated discontinuously in a "vortex sheet" the linear growth rate is

$$\Gamma = \tfrac{1}{2}|\boldsymbol{k}\cdot\boldsymbol{U}_o|[1-(2c_A\hat{\boldsymbol{k}}\cdot\hat{\boldsymbol{B}}_o)^2/(\hat{\boldsymbol{k}}\cdot\boldsymbol{U}_o)^2]^{1/2},$$

where $\boldsymbol{U}_o$ is the velocity difference between the two layers, c_A is the Alfvén speed, $\boldsymbol{k}$ is the wavevector, and $\hat{\boldsymbol{B}}_o^u$ is the direction of the magnetic field (Chandrasekhar 1961). From this, one also can see that a necessary condition for instability is $c_A < |(\hat{\boldsymbol{k}}\cdot\boldsymbol{U}_o)/(2\hat{\boldsymbol{k}}\cdot\hat{\boldsymbol{B}}_o)|$. The instability constraint on the Alfvein Mach number, M_A, is $M_A = U_o/c_A > 2$, when magnetic field, velocity, and perturbation wavevectors line up. If the shear layer is of finite thickness, Γ will generally fall below the value predicted above, with a maximum

[1] Department of Astronomy, University of Minnesota, Minneapolis, MN 55455; afrank@astro.spa.umn.edu.
[2] Department of Astronomy, University of Minnesota, Minneapolis, MN 55455; twj@astro.spa.umn.edu.
[3] Department of Astronomy and Space Science, Chungnam National University, Daejeon 305-764, Korea; ryu@sirius.chungnam.ac.kr.
[4] Minnesota Supercomputer Institute, University of Minnesota, Minneapolis, MN 55455; gaalaas@msi.umn.edu.

growth rate for wavenumbers $k \sim 1/a$, where a measures the width of the transition layer. Similarly, the finite width of the shear layer stabilizes very short wavelength modes, $1/k \ll a$, preventing the divergence in the linear growth rate that occurs for a discontinuity. It appears that the same constraint on c_A applies in the finite shear layer (Miura & Pritchett 1982, hereafter MP). Compressibility of the fluid also tends to reduce the growth of the instability. There has been much discussion in the literature about the existence or nonexistence of an upper limit of order unity to the sonic Mach number for KH unstable flows (see, e.g., Landau 1944; Miles 1957; Blumen 1970; Blumen, Drazin, & Billings 1975; Artola & Majda 1987; Miura 1990). Especially when one considers super-Alfvénic shear layers of finite thickness, it appears that there is no such limit, although the growth of the instability under highly supersonic conditions is generally much slower than the classical, incompressible result.

Even though these results tell us when to expect the MHD KH instability and when it might have time to develop fully, only nonlinear calculations can determine its consequences. In recent years a number of two-dimensional numerical studies have been published aiming at various aspects of the problem (see, e.g.,Tajima & Leboeuf 1980; Miura 1984, 1987, 1992; Wang & Robertson 1984; Wu 1986; Belle-Hamer, Fu, & Lee 1988; Belmont & Chanteur 1989), especially as it applies to Earth's magnetosphere. However, the nonlinear physics of MHD KH unstable flows is very complex, and studies have generally been too limited by computational constraints (low numerical resolution and insufficient dynamical time coverage) to answer basic questions definitively about either the important physical processes involved or the eventual fluid state.

In the present paper we take some steps to help remedy that situation. Our intent is to address some basic issues identifying the character of fluid and magnetic field interactions once the MHD KH instability becomes nonlinear. Thus, we consider only the idealized, periodic KH instability, postponing for now a study of the evolution of KH unstable MHD flows in more general and realistic settings. In this way, we hope subsequently to understand better how those less controlled flows are formed. As our starting point we use the very nice work by Miura (1984), who examined the evolution of some normal mode perturbations to an unstable MHD shear layer. That problem is both numerically well posed and leads to a straightforward evolution. The role of the magnetic field is most critical when it is aligned with the flow, so we shall focus on that configuration. This means that our simulations are strictly two-dimensional, leading to some important properties in the flows, especially as they apply to the evolution of the magnetic field. For example, for planar symmetry a regenerative dynamo action cannot develop to amplify the field (see, e.g., Zel'dovich 1957; Moffatt 1978). On the other hand, both two- and three-dimensional MHD turbulent flows cascade energy to larger wavenumbers (see, e.g., Pouquet 1978), whereas two-dimensional hydrodynamical turbulence produces an inverted energy cascade. A two-dimensional simulation, however, enables us to achieve high numerical resolution that can be crucial to obtaining solutions in which the large-scale motions and global statistical properties are not strongly influenced by numerical diffusion.

Since the character of the flow evolution is rather different for flows in which the initial magnetic field strength is large ($c_A \sim U_o$) than when it is small ($c_A \ll U_o$), we consider both of those cases. Miura's calculations were terminated shortly after the nonlinear saturation of the instability, because of concerns about numerical limitations and because the periodic version of the instability is idealized as already mentioned (see Wu 1986). On the other hand, understanding how the flow relaxes after saturation could be very useful in deciphering the fully nonlinear behavior of the instability in more general settings. So, we have extended our simulations until an approximate equilibrium is achieved. We note here that stable, equilibrium flows develop in these simulations on a much shorter timescale than that required to dissipate the kinetic energy in the initial configurations. Miura's calculations were carried out on a rather coarse numerical grid (100 × 100 zones), and he made no effort to examine the convergence of his results. On the other hand, the numerical evolution of complex flows is often highly dependent on numerical diffusion that effectively limits the Reynolds numbers in the flow. Mac Low et al. (1994) recently emphasized the special importance of this concern for MHD flows. Thus, we have carried out each of our simulations at two or more resolutions to provide some information about that issue. We note that Malagoli, Bodo, & Rosner (1996) have independently concluded a similar numerical study using different methods. Their results are entirely consistent with ours, and their discussion complements this one.

The plan of the paper is as follows: In § 2 we describe our numerical methods and the initial conditions used. Section 3 contains a discussion of the characteristics of the several phases of the evolution in the instability, while § 4 is a brief summary with conclusions.

2. METHODS AND INITIAL CONDITIONS

MHD describes the behavior of the combined system of a conducting fluid and magnetic field in the limit that the displacement current and the separation between ions and electrons are neglected. So, the MHD equations represent coupling of the equations of fluid dynamics with the Maxwell's equations of electrodynamics. When the effects of viscosity, electrical resistivity, and thermal conductivity can be neglected on large scales one works with the ideal, compressible MHD equations:

$$\frac{\partial \rho}{\partial t} + \nabla \cdot (\rho \boldsymbol{u}) = 0 , \tag{2.1}$$

$$\frac{\partial \boldsymbol{u}}{\partial t} + \boldsymbol{u} \cdot \nabla \boldsymbol{u} + \frac{1}{\rho} \nabla p - \frac{1}{\rho} (\nabla \times \boldsymbol{B}) \times \boldsymbol{B} = 0 , \tag{2.2}$$

$$\frac{\partial p}{\partial t} + \boldsymbol{u} \cdot \nabla p + \gamma p \nabla \cdot \boldsymbol{u} = 0 , \tag{2.3}$$

$$\frac{\partial \boldsymbol{B}}{\partial t} - \nabla \times (\boldsymbol{u} \times \boldsymbol{B}) = 0 , \tag{2.4}$$

along with the constraint $\nabla \cdot \boldsymbol{B} = 0$ imposed to account for the absence of magnetic monopoles (see, e.g., Priest 1984). The gas equation of state is $p \propto \rho^{\gamma}$, where ρ and p are the density and gas pressure. Standard symbols are used for other common quantities. Here, we have chosen rationalized units for the magnetic field so that the magnetic pressure $p_b = \frac{1}{2}B^2$, and the Alfvén speed is simply $c_A = B/\rho^{1/2}$.

These equations were solved numerically using a multidimensional MHD code based on the explicit, finite-difference

"total variation diminishing" or "TVD" scheme. That method is an MHD extension of the second-order finite-difference, upwinded, conservative gasdynamics scheme of Harten, as described by Ryu & Jones (1995). The multidimensional version of the code, along with a description of various one and two-dimensional flow tests is contained in Ryu, Jones, & Frank (1995). The code contains a fast Fourier transform–based routine that maintains the $\nabla \cdot \boldsymbol{B} = 0$ condition at each time step within machine accuracy.

Numerical solution of equations (2.1)–(2.4) on a discrete grid leads, of course, to diffusion of energy and momentum as well as to entropy generation. Of course, such effects are also present in nature and are important to defining the character of the flows. The existence of effective numerical resistivity is necessary, for example, to allow magnetic reconnection to occur. There is fairly good evidence that conservative monotonic schemes, as this one is, do a good job of approximately representing physical viscous and resistive dissipative processes that are expected to take place on scales smaller than the grid (see, e.g., Porter & Woodward 1994). For the astrophysical environments being simulated the expected dissipative scales are likely very much smaller than those that can be modeled directly. One anticipates, then, that increased numerical resolution leads to solutions in which the large-scale flow patterns "converge" in a statistical sense over timescales of interest, or in more detail over limited time intervals.

Our calculations are carried out in the $(x - y)$ plane with the initial background flow aligned with the x direction. For those simulations presented here we have used a computational space that is square and extends over $x = [0, L_x]$ and $y = [0, L_y]$, with $L_x = L_y = L$. In some related tests we applied different proportions for L_x and L_y. The calculations are formally of "$2 + \frac{1}{2}$" dimensions, since we can include the u_z and B_z components. In practice, however, $u_z = 0$ and $B_z = 0$ for the simulations we present here. We will consider the more general case elsewhere. Thus, the simulations are practically two-dimensional. Following MP, the computational domain is periodic in x, while the y boundaries are reflecting; i.e., both normal velocity and magnetic field change sign across the top and bottom boundaries. In addition, it is straightforward to show using equation (2.4) and the Stokes theorem that under these conditions we expect $(\partial \langle \boldsymbol{B} \rangle)/\partial t = 0$, where the brackets represent a spatial average over the computational domain. We have confirmed that this is exactly true in our simulations. The field is locally changing, of course, and the mean magnetic energy and pressure are variable, as well.

We consider an initial background flow of uniform density, $\rho = 1$, and gas pressure, $p = 0.6$, and an adiabatic index, $\gamma = 5/3$, so that the sound speed $c_s = (\gamma p/\rho)^{1/2} = 1.0$. The magnetic field, $\boldsymbol{B}_o = B_o \hat{\boldsymbol{x}}$, is also uniform, but its value is chosen to be either $B_o = 0.4$ or $B_o = 0.2$ in the two cases we have considered, as described below. The velocity in the background state is antisymmetric about $y = L/2$ according to the relation

$$\boldsymbol{u}_o = u_o(y)\hat{\boldsymbol{x}} = -\frac{U_o}{2} \tanh\left[\frac{y - (L/2)}{a}\right]\hat{\boldsymbol{x}}\,, \tag{2.5}$$

with $U_o = 1$. This describes a smoothly varying flow within a shear layer of full width $2a$. Flow is to the left in the top half-plane and to the right below that. To this state we add a perturbation, $\delta(\rho, p, \boldsymbol{u}, \boldsymbol{B})$. As in MP we define that perturbation to be a normal mode found from the linearized MHD equations, periodic in x and evanescent in y, with period equal to the length of the computational box L. Thus, each perturbed quantity can be expressed in a form

$$\delta f(x, y, t) = f(y) \exp(ik_x x + i\omega t)\,, \tag{2.6}$$

where each $f(y)$ is a complex function determined by numerical integration of the linearized MHD equations as outlined in MP. Physically, one requires the real part of each $\delta f(x, y, t)$, of course. Further, we have

$$k_x = \frac{2\pi}{L} \tag{2.7}$$

and

$$\omega = \omega_r - i\Gamma\,. \tag{2.8}$$

From symmetry the real frequency, ω_r, is zero in the computational frame, so that disturbances remain stationary as they evolve. The growth rate, Γ, can be computed by iteration on the solution for the f's, although we found it adequate to obtain Γ from the published figures in MP. Other parameters that characterize the system are the Alfvénic Mach number, $M_A = U_o/c_A$, and the sonic Mach number, $M_s = U_o/c_s$. It is common and convenient also to use the parameter $\beta = p_g/p_b = 6/5(M_A/M_s)^2$, to measure the relative importance of thermal and magnetic pressures. For the initial conditions given above we have $M_s = 1$ and either $M_A = 2.5$ ($\beta = 7.5$) or $M_A = 5$ ($\beta = 30$). These properties are summarized in Table 1. To minimize the influence of the reflecting boundaries we followed Miura's (1984) prescription to keep $L \geq 20a$. For the simulations presented here, $L = 25a$. With this scale boundary zone errors in the initial normal mode perturbation are insignificant. It is most convenient in using MP's formulation to determine the various perturbed variables from a solution to δp^*, where $p^* = p + p_b$. Beginning with an initial value of δp^* at one of the y boundaries, one can integrate to the midplane and then extend the solution to the other boundary using appropriate even or odd symmetries for the flow variables around a pair of symmetry nodes along the line of flow symmetry. In the two cases presented, we used $\delta p^*(y = L) = 0.001 p_o^*$, ($M_A = 2.5$), and $\delta p^*(y = L) = 0.01 p_o^*$, ($M_A = 5$). The node points were $y = L/2$, $x = L/4$, $3L/4$. From the initial conditions (background state + perturbations) we allowed the unstable flow to evolve until it approached an apparently relaxed state. In practice this meant running the simulations for up to 20 linear growth times; i.e., $\tau = 20t/t_g$, where $t_g = \Gamma^{-1}$.

To understand better how well our solutions are numerically converged in the sense described near the beginning of this section, we computed each case on the above domains using several different resolutions. Each case was computed on both 256×256 and 512×512 grids. In addition, the $M_A = 5$ case was carried out on a 128×128 grid. The

TABLE 1

CALCULATION INITIAL PARAMETERS

Model	U_o	B_o	a	M_s	M_A	β	Γ
Strong field.....	1	0.4	$L/25$	1	2.5	7.5	$0.053(U_o/2a)$
Weak field.....	1	0.2	$L/25$	1	5	30	$0.108(U_o/2a)$

highest resolution simulations required between 20 and 40 CPU hours on a Cray C90 computer. Setting $\lambda = 2\pi/k_x = L$ maximizes our ability to resolve structures small compared to the initial perturbed wavelength. On the other hand, one might be concerned that important structures should form on scales longer than the initial perturbation wavelength. That is not possible when $\lambda = L$, of course. To evaluate this concern we repeated the 256 × 256, $M_A = 5$ simulation on a $x = [0, 2L]$, $y = [0, L]$ domain using a 512 × 256 grid. In other words, we extended the computational box to include two perturbation wavelengths but kept everything else unchanged. The results were indistinguishable from the simulation on the square box, so we conclude that no important information of this type has been lost by letting the perturbation wavelength match the box length. We should emphasize, of course, that the choice of periodic boundaries has itself restricted possible Fourier components, prohibiting the kind of large-scale coalescent structures noted by Wu (1986), for example. So, as pointed out by Wu, a study designed to predict the detailed structures in an unstable, convected shear layer at an arbitrary stage would need a different kind of symmetry.

We conducted one additional set of tests to evaluate a related issue; namely the influence of the location of the reflecting boundaries. Here, we doubled the distance to the reflecting boundary, $y = [0, 2L]$. In this case we concluded that the general properties of the flows were unchanged, especially within the central, strongly sheared region. Some structural details were slightly changed, but not sufficiently to alter any of the conclusions we will present below.

In summary, on a space periodic in one direction we computed the evolution of two uniform density, but compressible MHD KH unstable shear layers through their initial exponential growth, saturation, and nonlinear relaxation phases. Both cases had in common an initial magnetic field aligned with the fluid flow and a sonic Mach number for the velocity spread, $M_s = 1$. The two cases were distinguished only by the Alfvénic Mach numbers; those being $M_A = 2.5$ and $M_A = 5$. Although these Alfvénic Mach numbers differ by just a factor of 2, the flows are qualitatively very different.

3. RESULTS

3.1. *Overview: Weak-Field and Strong-Field Conditions*

Before discussing the two MHD shear layers we have studied it is useful to outline very briefly the well-known behavior in a two-dimensional gasdynamic, unstable shear layer (see, e.g., Maslowe 1981). For comparison we carried out a simulation equivalent to the MHD cases described here, except that the magnetic field was absent. In that case the perturbation, once it becomes nonlinear, quickly evolves into a single, large vortex that extends across the full length, L, of the grid. The vortex is flattened in y, so that it spans about $\frac{1}{3}$ of the grid in that direction. Since numerical viscosity is small, the fully formed, elongated vortex, sometimes called "Kelvin's Cat's Eye," is stable and would spin almost indefinitely. It becomes the only identifiable structure in the flow. Considering the periodic nature of the computational space, there would in the gasdynamic situation be a periodic line of vortices separating the two oppositely moving and mostly undisturbed fluids. For nonperiodic flow, vortex coalescence would lead to merging of these structures (see, e.g., Corcos & Sherman 1984). Eventually, over a timescale several orders of magnitude longer than we have considered, numerical viscosity would dissipate the vortex flow and the initial kinetic energy would be converted into thermal energy. That history, as we shall see, is rather different from what happens in either of the MHD flows we studied.

A sense of the evolutionary histories of MHD cases can be obtained by examining the transverse velocity u_y. Initially, that is just the perturbation δu_y. Figures 1*a* and 1*b* show the spatial rms values, $(\langle u_y^2 \rangle)^{1/2}$, for both cases as functions of time, given in units of the predicted growth times; i.e., $\tau = t\Gamma$. The different curves represent the various numerical resolutions used. Velocities are normalized by the initial value found for the perturbation in each run. Several key features are immediately evident. First, for both cases the amplitude, $(\langle u_y^2 \rangle)^{1/2}$, initially increases exponentially as expected, with a growth rate close to the theoretical value (shown by the short dashed line in each panel). For the $M_A = 2.5$ case there is a startup error that disturbs the growth momentarily, but it then resumes the predicted rate very closely. The error, which we attribute to the way our code's Riemann solver handled the initial conditions at one point along the midplane, is greater at the lower resolution, and it disturbed an even lower resolution run (128 × 128 grid) sufficiently that we elected to ignore those results. The second point to be made from Figure 1 is that after only a few linear growth times, $(\langle u_y^2 \rangle)^{1/2}$ saturates and then relaxes toward values that are below the initial perturbed levels. That "final," "relaxed" state has some interesting properties, so we shall return shortly to discuss it in some detail. The relaxed states that develop are analogous to the long-lived stable vortex described for gasdynamics. Since that state cannot be the ultimate condition for these flows in the presence of finite dissipation, we will refer to it as a "quasi-steady" relaxed state. We also note that the time for an initial perturbation to reach saturation depends on the amplitude of the perturbation. However, the time elapsed from saturation, measured in units of τ, ought to be characteristic of the properties of the unperturbed configuration, including the symmetry. This last statement comes from the observation that for a given background flow the characteristic global properties when the perturbation saturates are not very sensitive to the details of the perturbation itself. This is demonstrated for the present case by the good agreement between the saturation-phase flow properties seen in our simulations and those of Malagoli et al. (1996). The latter authors used a simple periodic velocity perturbation rather than a linear normal mode.

The third point from this figure is that the flow evolution is considerably more complex in the $M_A = 5$ case than in the $M_A = 2.5$ case. The difference in flows is even more obvious in the images of gas density and magnetic field lines displayed from our highest resolution runs in Figures 2 and 3. To facilitate visualizing the extension of structures on the periodic space we doubled each image. For the $M_A = 2.5$ case flows remain relatively laminar throughout and qualitatively resemble the initial, simply periodic form well past the stage when a linear description becomes invalid. The magnetic field lines as shown in Figure 2*b* suffer relatively modest bending or stretching. There is no indication of magnetic reconnection, nor that any suitable field topology for that process has formed. Once the oscillations reach their maximum amplitude, the flow seems simply to flatten out into a broadened shear layer. In marked contrast, the

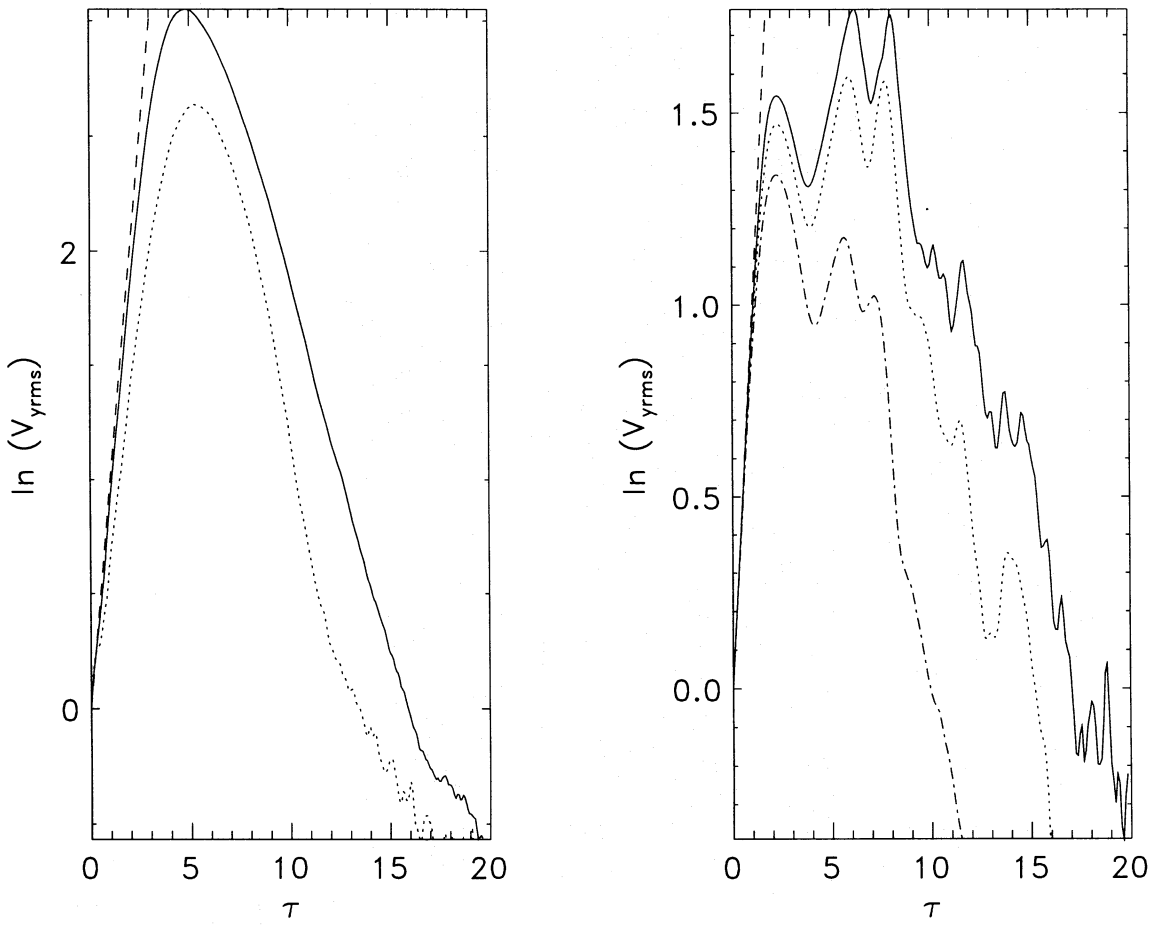

FIG. 1.—Evolution of spatially averaged rms transverse velocities normalized by their initial values. Shown are the natural logarithm of the square root of the average u_y^2 throughout the evolution of the (*a*) strong-field case and (*b*) weak-field case. The solid, dotted, and dashed-dotted lines correspond to the high (512^2), medium (256^2), and low (128^2) resolution simulations, respectively.

$M_A = 5$ case develops flows that become quite complex, with distinct, intermittent vortices. The large-amplitude oscillations in $(\langle u_y^2 \rangle)^{1/2}$ after $\tau \approx 2$ are associated with the generation and decay of these vortex structures. The large "primary vortex" centered on $x = 3L/4$ at the $\tau = 2.4$ in Figure 3 reaches its maximum development after $\tau = 2$ and corresponds to the first maximum in $(\langle u_y^2 \rangle)^{1/2}$. Around $\tau = 6$ the magnetic field lines on the outside of that vortex, having been wrapped back on themselves, tear in a major reconnection event that matches with the second maximum in $(\langle u_y^2 \rangle)^{1/2}$. Figure 3*b* shows the field configuration at $\tau = 5.6$, just before that event. The third maximum in $(\langle u_y^2 \rangle)^{1/2}$ corresponds to a similar reconnection event associated with the well-formed "secondary vortex" centered at $x = L/4$ and $\tau = 8$ in Figure 3. Smaller peaks in $(\langle u_y^2 \rangle)^{1/2}$ can also be seen at $\tau \approx 12$, 15, and 18. Each is associated with reconnection in a vortex structure within the flow.

There are clear differences between the descriptions just given for the MHD flows and that presented earlier for the analogous gasdynamic situation. Even when the magnetic field is initially weak its presence becomes crucial in determining the nonlinear evolution of the flow. The initially weak field is able to mediate dynamical and dissipative processes through local growth and decay. Not surprisingly, the role played early on by the magnetic field depends considerably on its initial strength. That is apparent in the initial, exponential growth rates. The growth rate for the $M_A = 5$ case [$\Gamma = 0.108 \times (U_o/2a)$] is about 90% of the purely hydrodynamic rate [$\Gamma = 0.122 \times (U_o/2a)$; Miura & Pritchett 1982], whereas the rate for the $M_A = 2.5$ case [$\Gamma = 0.053 \times (U_o/2a)$] is less than half the (same) hydrodynamic rate. From these various contrasts it is convenient and, we believe appropriate, to distinguish in our remaining discussion the two cases as "weak field" ($M_A = 5$) and "strong field" ($M_A = 2.5$), thus being generally representative of qualitatively different flows. Malagoli et al. (1996) also saw a qualitative transition in properties between these two field strengths. We note for comparison that the incompressible hydrodynamical linear perturbation growth rate of a discontinuous shear layer is $\Gamma = \pi \times (U_o/\lambda)$. Here, $\lambda = 25a$ [$\Gamma \rightarrow (\pi/12.5) \times (U_o/2a)$], so a combination of compressibility and the finite spread in the shear layer has reduced the initial growth rate by more than a factor of 2 even before Maxwell stresses are introduced. The sonic Mach number is unity, after all, and in each case thermal energy is globally the dominant energy form throughout the simulations by about an order of magnitude.

As noted before, numerical resolution is an important issue in evaluating computations of this kind. We will comment on specific resolution-related questions as they come up, but we can make some preliminary observations here. It is clear from an examination of Figure 1 and by comparing images of various physical quantities, that many qualitative behaviors are similarly captured in all of the calculations. In Figure 1*b*, for example, the same major

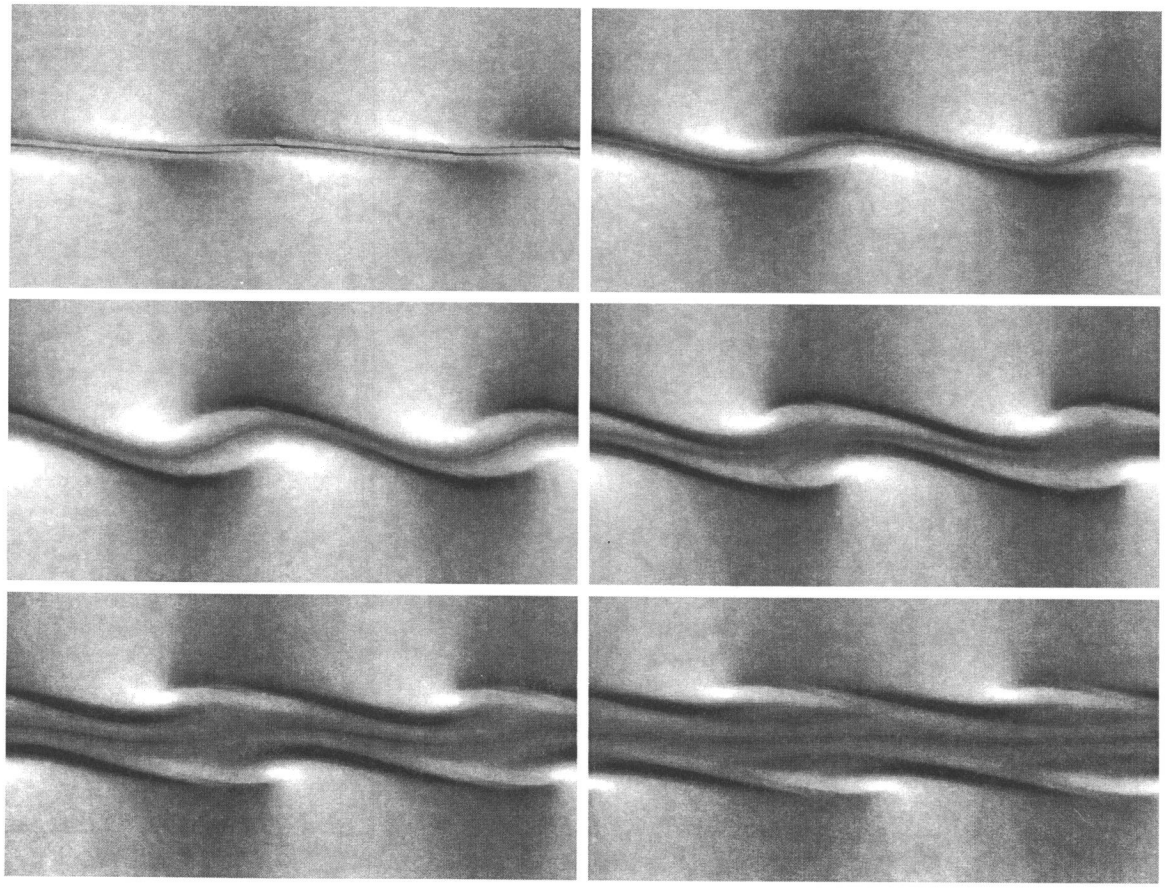

Fig. 2*a*

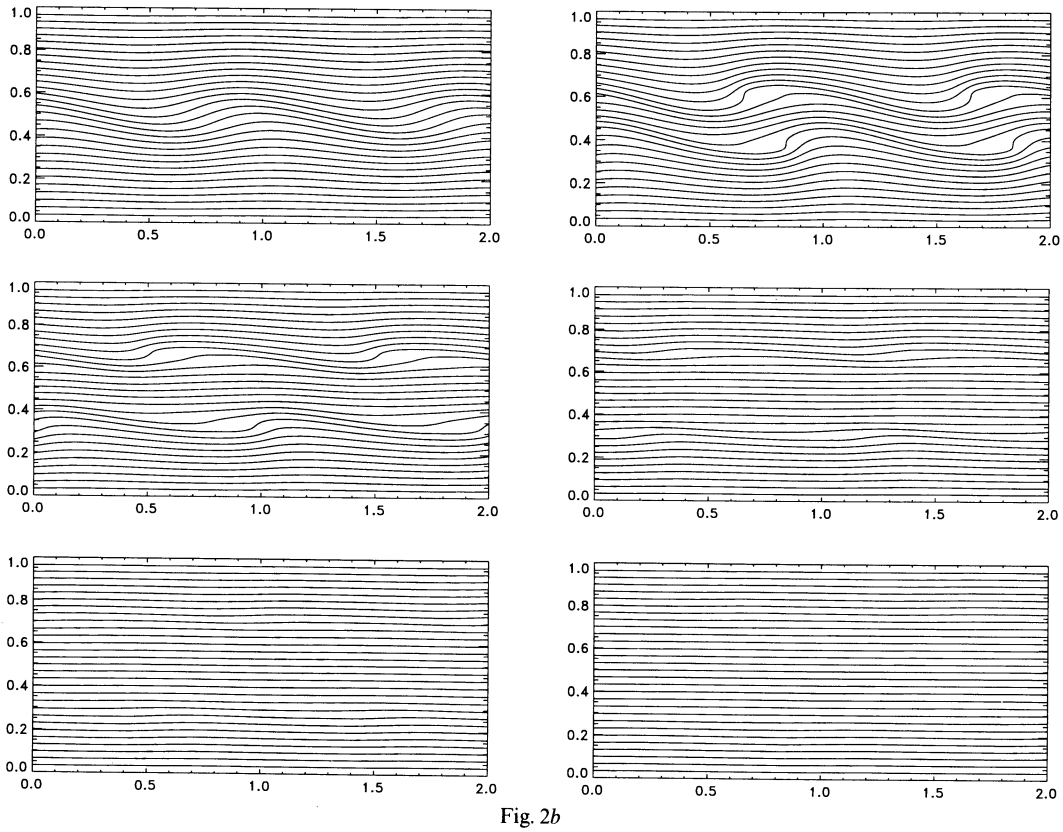

Fig. 2*b*

FIG. 2.—Gas density (*a*) and magnetic field lines (*b*) at 6 times in the evolution of the high-resolution strong-field simulation. The gas density is shown as gray-scale images, where dark regions correspond to low values. To facilitate visualization of periodic structures across the boundaries each image has been doubled. Coordinate values, measured from the lower left are in units of L. The times shown are 3.0, 6.0, 9.0, 11.9, 14.9, and 17.9 in units of $\tau = t/\Gamma^{-1}$.

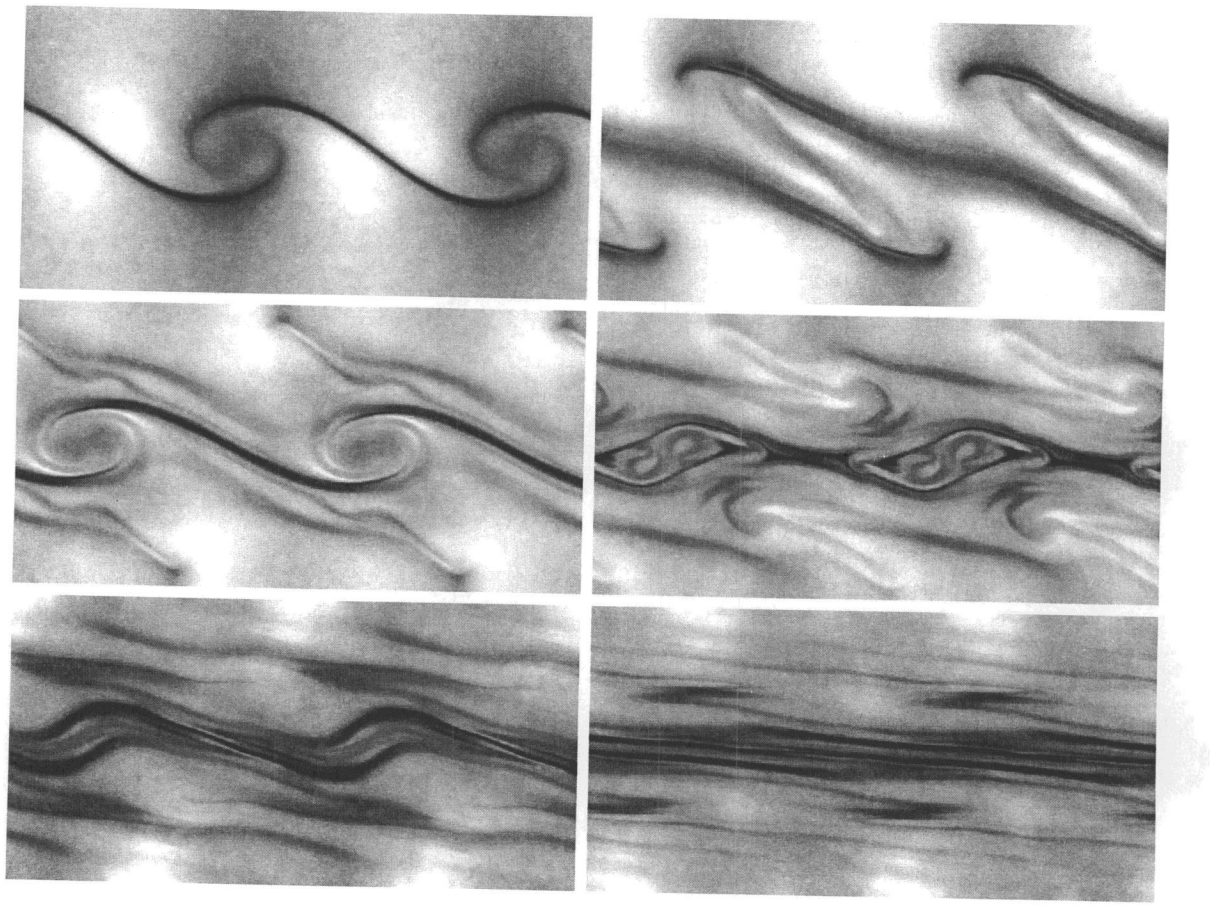

Fig. 3*a*

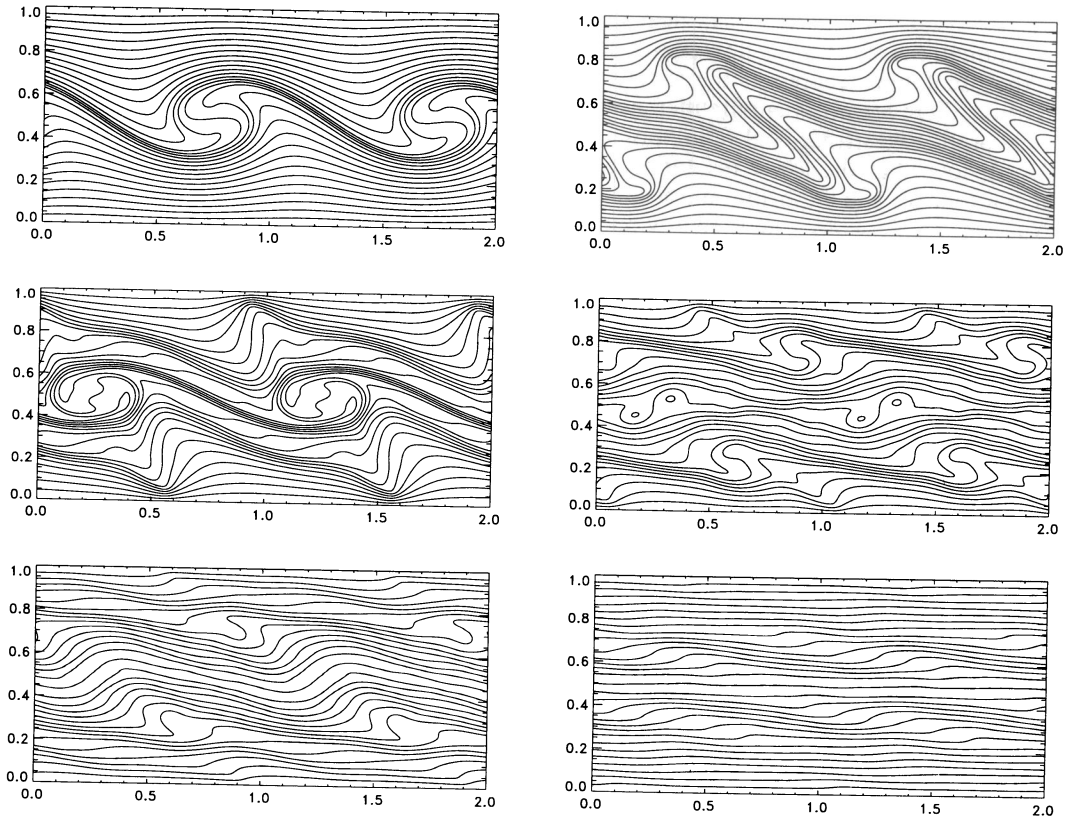

Fig. 3*b*

FIG. 3.—Gas density (*a*), magnetic field lines (*b*), and velocity field (*c*) at 6 times in the evolution of the highest resolution weak-field simulation. Presentation is similar to Fig. 2. The velocity field is shown as vectors. The times shown are 2.4, 5.6, 8.0, 10.4, 14.4, and 20.0 in units of $\tau = t/\Gamma^{-1}$.

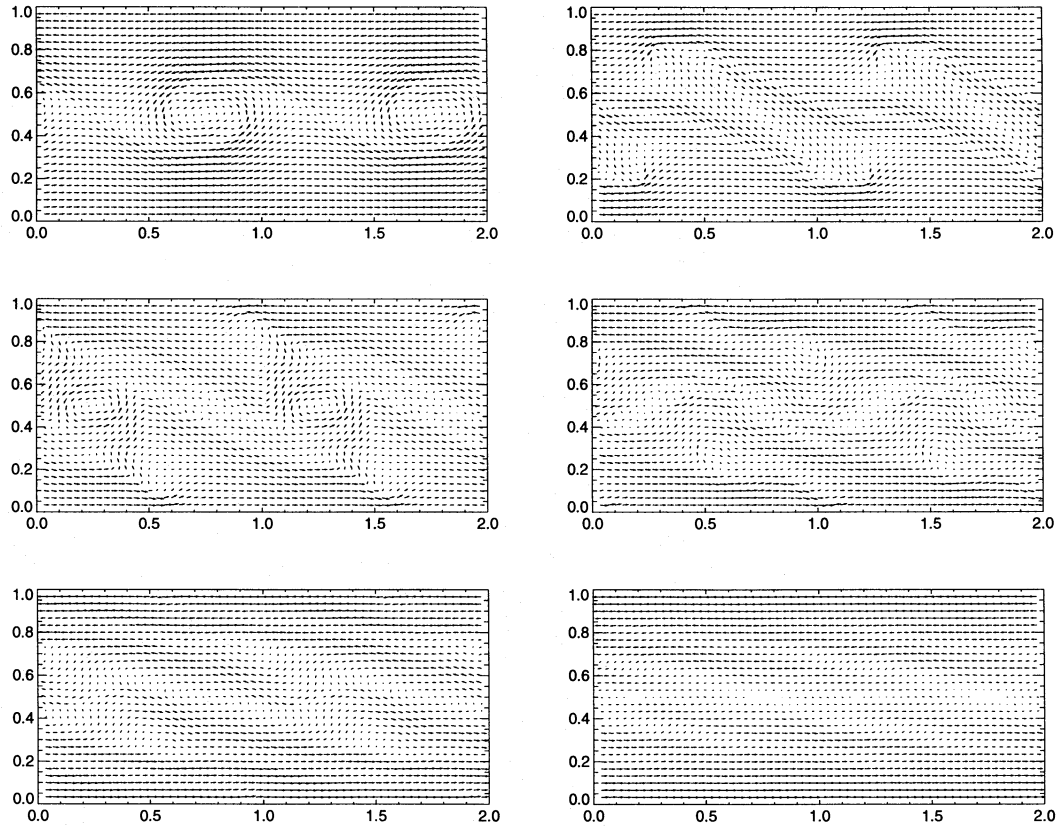

Fig. 3*c*

oscillations in $(\langle u_y^2 \rangle)^{1/2}$ occur for all three weak-field simulations. By viewing animations of the three-flow simulations one can see that the oscillations represent the same flow events as well. Likewise, there are no essential differences in the global characters of the two strong-field simulations. At the same time it is obvious that the lower resolution runs are not converged quantitatively in important physical variables such as peak magnetic energy or kinetic energy during the saturation phase. Ryu et al. (1995) demonstrated with this code that under conditions similar to the strong-field case here, isolated structures need to be resolved within about 30 zones before one can realistically neglect numerical diffusion; i.e., before the effective "Reynolds number" of the structures greater than 10^3. For conditions similar to the weak-field case that requirement is somewhat less restrictive. There we can estimate that about 20 zones are needed. Thus, while our lowest resolution runs would contain as few as six "fully resolved" structures in each direction, that number climbs to around 25 or more in the highest resolution simulations.

We will now proceed to discuss the characteristics of three phases in the nonlinear evolution of the simulated flows. From the preceding outline we identify these as (1) saturation, (2) relaxation, and (3) the quasi-steady, relaxed state. The initial, exponential growth phase is simply an extension to larger amplitude of the initial perturbation as discussed in MP, so we will not discuss it here. The quasi-steady relaxed state is relatively simpler than any of the other nonlinear stages and comes closest to having conditions that are straightforward to predict. Consequently, we begin our analysis there.

3.2. *The Quasi-steady, Relaxed State*

As mentioned in the previous summary, the simulated flows in both strong- and weak-field cases relax fairly quickly to an apparently steady condition. The fact that we have used periodic boundaries in our simulations and have conserved total energy in the domain of computation means that eventually the flow kinetic energy must be dissipated. But, that ultimately anticipated condition is not what is observed here, as emphasized by the comparison made with the gasdynamic case. The final density and magnetic field structures in our MHD simulations as shown at $\tau = 17.9$ for the strong-field flow in Figure 2 and at $\tau = 20$ for the weak-field flow in Figure 3 give a sense of the character of the relaxed states reached. The flows are nearly laminar, reflecting the fact that the mean transverse velocity has decayed to very small levels by this time (see Fig. 1). There are remaining visible striations in both the density and magnetic fields, however (see also Fig. 4). Within the magnetic field variations the magnetic and velocity fields are almost perfectly aligned, so that the normalized cross helicity,

$$\langle H \rangle = \frac{\int \hat{\boldsymbol{u}} \cdot \hat{\boldsymbol{B}} dx\, dy}{\int dx\, dy}, \tag{3.1}$$

very closely approaches the possible extrema, ∓ 1, in the top and bottom half-planes, respectively. Thus, the flows are highly organized by this time. Initially, the cross helicity is also large, but for the weak-field flow it becomes much reduced during the nonlinear phases of flow evolution. In that case the maximized cross helicity at the end may be related to so-called "dynamical alignment," first noted with

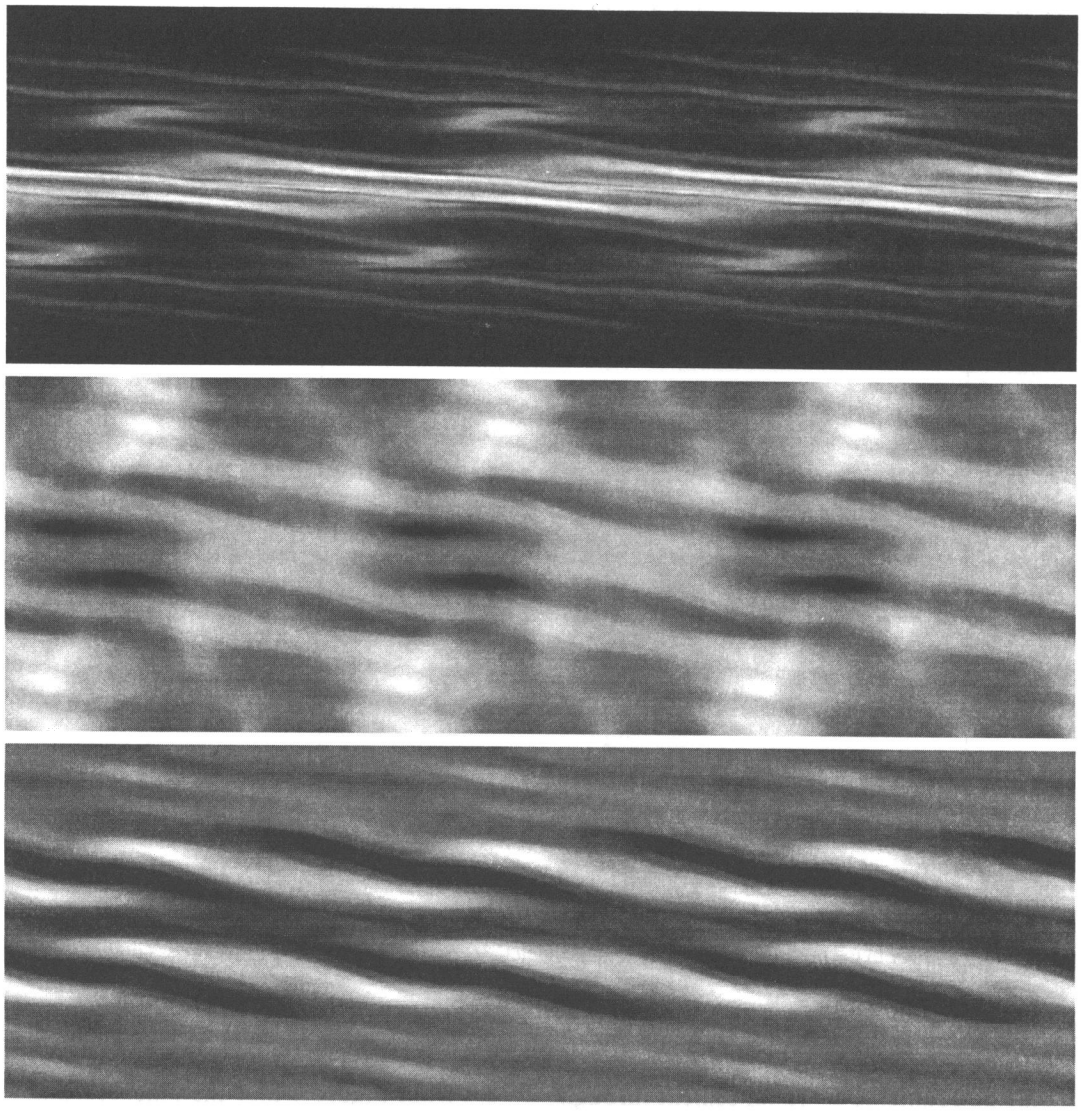

FIG. 4.—Gray-scale images (*top to bottom*) of the entropy, gas, and magnetic pressures at the end of the weak-field run (t = 20τ). Dark correspond to low values. To facilitate visualization on the periodic space, each image has been tripled.

respect to similar characteristics in the solar wind by Dobrowolny, Mangeney, & Veltri (1980), and subsequently examined theoretically and numerically in more general contexts of MHD turbulence (see, e.g., Pouquet, Meneguzzi & Frisch 1986; Ting, Matthaeus, & Montgomery 1986). Outside of the small influences of the striations, the transverse velocity gradients, $\partial u_x/\partial y$, are almost constant within the broadened shear layer. We have examined animations of a number of variables to ascertain any remaining trends in the flow evolution. Although it is apparent that some of the feature details may be expected to relax further, it seems clear to us that the general properties of the flow patterns visible at these times will continue to exist as seen well beyond the end points of our simulations and that no new features are developing.

The properties of the magnetic field in the relaxed states are perhaps the easiest to understand. They come largely from the assumed symmetry in the problem and the laminar nature of the flow in the relaxed states. $\langle B_x \rangle$ and $\langle B_y \rangle$ are both exactly conserved during the calculation, so in the relaxed states we may expect fairly uniform fields. The magnetic energy in the flow may be reasonably expected to return to something resembling its original value. The manner of those trends can be made evident by using equation (2.4) to derive a relation for the evolution in the mean magnetic energy density, $\langle E_b \rangle = \frac{1}{2}\langle B^2 \rangle$. As mentioned in the introduction we depend on numerical dissipation to mimic the effects of viscosity and resistivity, although we cannot describe an analytic model for the two effects or accurately separate them. However, to understand heuristically their effects qualitatively we can add a term $\eta \nabla^2 \boldsymbol{B}$ to equation (2.4), where η represents the effects of numerical resistivity. For a two-dimensional flow with our boundary conditions this leads to the equation

$$\frac{d\langle E_b \rangle}{dt} = \frac{\partial \langle E_b \rangle}{\partial t} + \langle (\boldsymbol{u} \cdot \nabla) E_b \rangle$$

$$= -\eta \langle j^2 \rangle - \langle 2E_b \nabla \cdot u \rangle + \langle \boldsymbol{B} \cdot [\boldsymbol{B} \cdot \nabla u] \rangle , \quad (3.2)$$

where $\boldsymbol{j} = \nabla \times \boldsymbol{B}$ is the current density and we assumed η to be constant. The average is over the entire domain. The three right-hand terms represent, respectively, Joule dissipation or magnetic diffusion, compression of the field and field line stretching. Unless the relaxed field configuration is

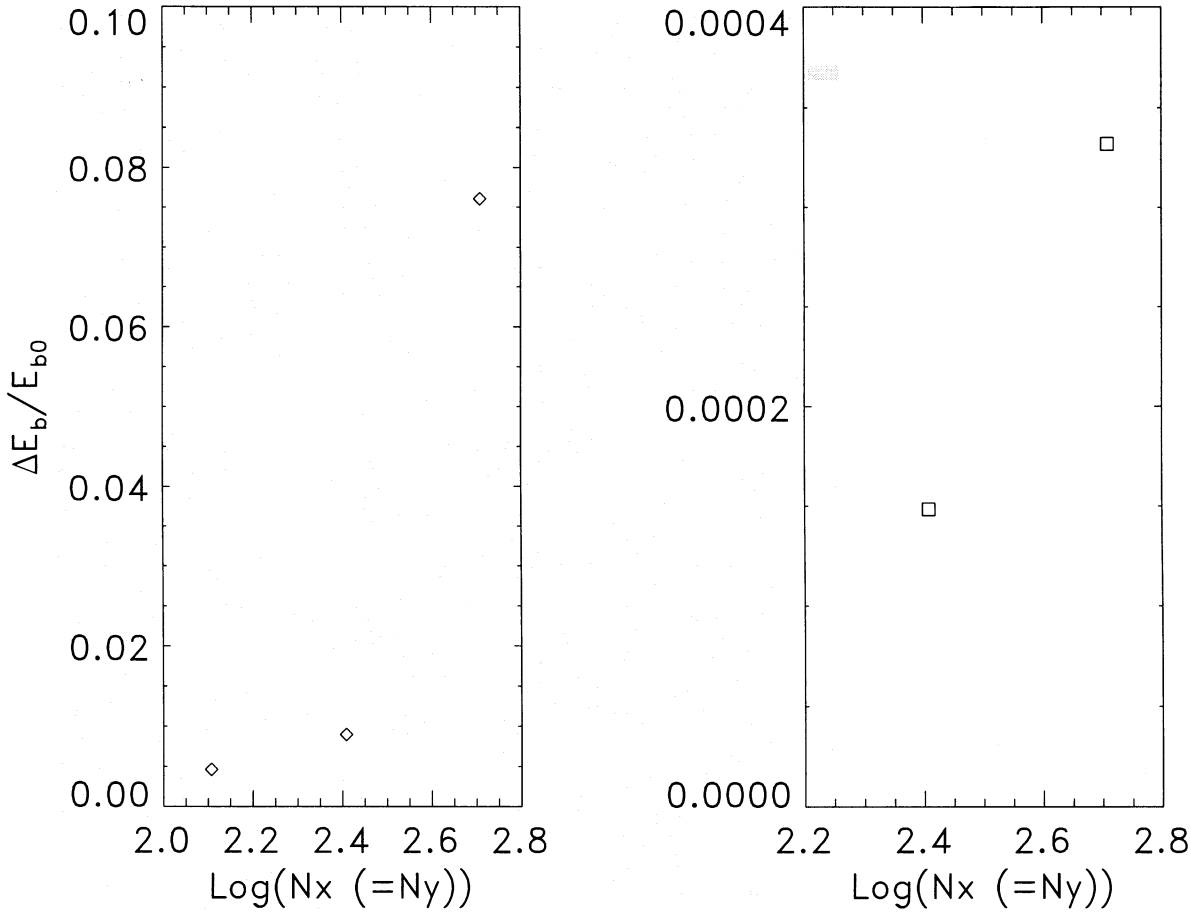

FIG. 5.—Fractional difference in magnetic energy between initial and final states in simulations as a function of resolution. Shown are $(E_{bf} - E_{bo})/E_{bo}$, where the subscripts "f" and "o" refer to the final and initial values of the magnetic energy. Note the units on the abscissa in the strong-field case.

uniform there will ordinarily be a finite $\langle j^2 \rangle$ and hence dissipation. That term always will decrease the magnetic energy and can only be countered by enhancement through compression and stretching. But in the laminar relaxed state those effects are fairly small, because of the absence of strong gradients in the velocity structure. Thus, we must expect that the final field will be relatively uniform and that the associated magnetic energy will resemble the initial value in order to satisfy the constant mean field values.

Figure 5 shows the fractional change between the initial and final magnetic energies, $\Delta E_b/E_{bo}$, for both the strong and weak-field cases as a function of the number of grid points, N_x, used in the various simulations. We see that for the strong-field case the final and initial magnetic energies are, indeed, almost precisely the same for both numerical resolutions used. They agree to much better than 1%. For the weak-field case, the two lower resolution simulations also relax to a state with magnetic energy equaling the initial value to better than 1%. Remarkably, however, the highest resolution simulation in this case ends with a magnetic energy greater than the initial value by about 7.7%. Figure 6, which shows the time evolution of $\langle B_x^2 \rangle$ and $\langle B_y^2 \rangle$ for that simulation, also illustrates this fact. Although $\langle B_y^2 \rangle$ returns very close to its initial value, $\langle B_x^2 \rangle$ does not evidently do so. We cannot rule out the possibility that $\langle B_x^2 \rangle$ will slowly decay to its initial value, but we prefer another interpretation of this result; namely, that it represents the initial development of "two-dimensional flux tubes." Figure 4 shows that the final state in this flow contains a pair of broad striations in enhanced magnetic pressure positioned on opposite sides of the midplane, $y = L/2$. It is also apparent from Figure 4 that the magnetic and gas pressure distributions are strongly anticorrelated at this time. Moreover, the maxima in magnetic pressure are also local minima in gas density. These features can, therefore, be

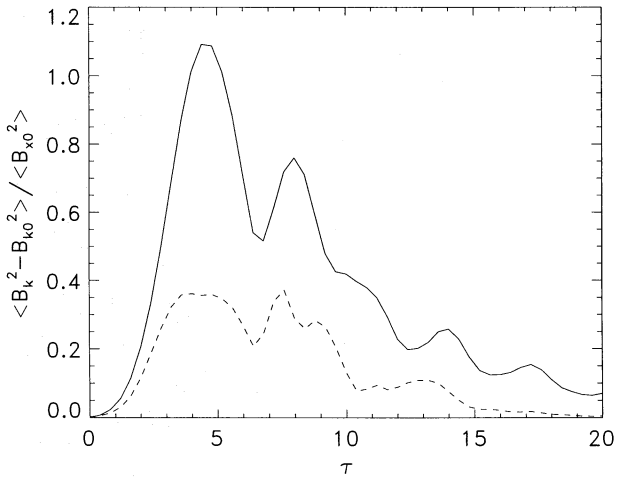

FIG. 6.—Evolution of the spatially averaged squared magnetic field components for the highest resolution weak-field simulation. Shown are the values of $\langle (B_k - B_{k0})^2 \rangle$, where $k = x, y$, are indices. They are normalized to the initial x component squared, $(B_{x0})^2$. The solid and dotted lines show the evolution of the x, and y components, respectively.

described as slow mode rarefactions, similar to the "plasma depletion" zone described for an earlier stage of the flow by Miura. In addition, we already mentioned that the velocity and magnetic field vectors are almost exactly parallel in the lower half-plane and antiparallel in the upper half-plane. Thus, the magnetic field lines and velocity streamlines are aligned, and the flow is directed along the tubes. By watching animations of the evolution of the magnetic field structure one can see that the two flux tubes (stronger field regions) have survived as coherent features since the reconnection event associated with the breakup of the large vortex. The tubes can be identified relatively easily as clusters of field lines stretching obliquely above and below the vortex in the $\tau = 8$ panel of Figure 3*b*. From that time they gradually settle down toward the midplane as activity in that region decays. We see no evidence of these tubes as coherent structures in our lower resolution simulations of this flow. Numerical diffusion presumably prevented them from forming, a fact that emphasizes the need for adequate numerical resolution in simulations of this type. There is also no indication of such structures in the strong-field case, because there were no opportunities for dynamical self-reorganization through magnetic reconnection during evolution of that flow.

These final structures are also apparent in the Fourier power spectrum of the magnetic pressure, p_b. We constructed two-dimensional power spectra, $P^b_{x,y}$, at a number of times for both the magnetic field cases. The power spectra are not isotropic, as obvious from the flow structures seen in Figs. 2 and 3. Initially, P^b_x, the power spectrum along different k_x, has a single mode at $k_x = 1$ of course. P^b_y, the power spectrum along different k_y, has a fairly broad distribution at the beginning, reflecting the finite thickness of the shear layer. At the end of the simulations, P^b_x has returned to have almost a monochromatic mode for both cases. For the strong-field case P^b_y is also similar to its initial form, but with two notable changes. The dominant mode is now at $k_y = 3$ rather than at $k_y = 1$. In addition, it is spread over more modes to reflect an increased thickness of the shear layer, and there is some structure in the power spectrum coming from the features that can be seen in Figure 2. In the weak-field case P^b_y has a narrower peak than that at the beginning with the dominant power at $k_y = 4$, but also with distinct peaks at $k_y = 8$ and 12. Some power extends to the highest modes in this case, as expected from thin stripes seen in Figure 3.

As already mentioned, except for small deviations aligned with remaining magnetic features, the final velocity structure can be described as a simple shear layer (see Fig. 3*c*). During the evolution of the flow the initial shear layer spreads, of course, because momentum is transported between the bottom and top halves of the computational domain. Horizontal momentum, ρu_x, is transported in the y direction by way of Reynolds stresses, $\rho u_x u_y$, Maxwell stresses, $B_x B_y$, and also by numerical diffusion. In the same spirit as we had for equation (3.2), we can represent that last behavior qualitatively in terms of an effective viscous stress, σ_{xy}, (see, e.g., Landau & Lifshitz 1987). Then, for example, using the symmetry and boundary properties of this problem the change in the mean ρu_x within the *upper half* of the domain is

$$\frac{\partial \langle \rho u_x \rangle}{\partial t} = \frac{2}{L^2}\left[\int_o^L (\rho u_x u_y - B_x B_y + \sigma_{xy}) dx \bigg|_y = \frac{L}{2}\right] \quad (3.3)$$

(see also Miura 1984). The shear layer should spread so long as $\partial \langle \rho u_x \rangle / \partial t > 0$, since initially $\langle \rho u_x \rangle < 0$ in this region. Once the flow becomes nearly laminar the Reynolds and Maxwell stress contributions to momentum flux across the midplane should become small, leaving only the viscous stresses as a source of transport. Although viscous stresses can never be entirely eliminated, they can be reduced to nominal levels as the numerical resolution is increased. For our highest resolution runs of both cases the momentum flux as measured by the right-hand side of equation (3.3) is very small for $\tau > 10$. It is almost exactly zero in the strong-field case, but oscillates around zero with decreasing amplitude in the weak-field case.

As the disturbed flows become nearly laminar, shear layer spreading slows for reasons just given. We will address in § 3.3 how that return to near laminar flow happens. But, one might reasonably ask why remaining fluctuations in u_y do not lead to renewed growth and further spreading as that final state is approached. Qualitatively, at least, the answer seems straightforward. In particular, if we note that the u_x structure of the final state is similar to that in the initial flow except for the width in y, then we know from the linear dispersion relation (e.g., MP) that there is a minimum unstable wavelength related to the thickness of the shear layer; i.e., for unstable perturbations, $k < \phi/2a$, where $\phi \sim 1 - 2$, depending on M_A and M_s. The fastest growing modes are concentrated at wavenumbers about half this limit. On the other hand, our periodic boundary conditions limit Fourier components in the flow to $k \geq 2\pi/L$. Thus, we expect that once the shear layer has spread so that the nominal width, $a \sim |U_o/(\partial u_x/\partial y)| > \phi L/4\pi$, a quasi-laminar flow will be mostly stable to any further perturbation, independent of the magnetic field strength. For both cases we studied the final shear layer width as estimated from the slope of the central region is at least $\sim 0.5L$. So, from the conditions just derived, we would not expect renewed growth. For the weak-field case this estimated final value of a from the observed flow is $\sim L$, which could be limited or modified by boundary effects. As further confirmation of our conclusion, then, we carried out a 256×256 simulation using $L_x = L_y = 2L = 2\lambda$. Except for details in the flows near the top and bottom boundaries the properties of that flow were the same as for the 128×128 simulation using $L_x = L_y = L = \lambda$.

We previously noted that in the relaxed state the magnetic field lines and flow streamlines are highly correlated. That is evident in Figures 3*b* and 3*c*. In fact, it is apparent that within the "flux tubes" velocity and magnetic field fluctuations satisfy the relation $\delta \boldsymbol{u} \sim \mp \delta \boldsymbol{B}$, where the minus sign corresponds to the fluctuations in the upper half-plane and the plus sign corresponds to the lower half-plane. That relation is consistent with the remaining fluctuations being carried in Alfvén waves that propagate locally downstream within the flux tubes and are linearly polarized so that $\delta u_z = \delta B_z = 0$. This feature and the convergence and divergence of flow along the varying width of the tubes explains the good correlation of magnetic pressure and u^2 observed when the velocity is corrected for the mean shear structure $\langle u_x(y) \rangle$.

In contrast to the magnetic energy, we should anticipate that the final total kinetic energy inside the computational domain, E_k, will be reduced in response to the relaxation of the flows. Since in the relaxed flow the velocity transition is spread out more between the top and bottom states, and the

computation was carried out in the center-of-momentum frame, we can expect that the quantity $\langle u_x^2 \rangle$ is reduced over the domain by the spreading of the transition. In both the strong- and weak-field cases the kinetic energy in the relaxed state exceeds the magnetic energy. For the strong-field case $E_k/E_b \approx 1.09$ at the end of the simulation. It is conceivable that an eventual fairly long-term equipartition between magnetic and kinetic energy develops. However, kinetic energy in the weak-field flow always significantly exceeds magnetic energy in our simulation. In the relaxed state $E_k/E_b \approx 2$. On a much longer time frame, it is not inconceivable that an equipartition between kinetic and magnetic energies develops in response to the dissipative decay of the flow mentioned in the next paragraph. On the other hand, it is also possible that the observed non-equipartition condition *does* represent the relaxed condition of the flow. Ting et al. (1986) have pointed out that turbulent MHD flows dominated by dynamical alignment can trend to long-term states in which the kinetic energy remains dominant over the magnetic energy.

Since the magnetic energy is little changed at the end from the beginning and kinetic energy is reduced, it follows that the final states must possess increased thermal energy over the initial flows. Figures 7 and 8, which display the evolution of the total kinetic, magnetic, and thermal energy forms over time, verify this. For the strong-field case the kinetic energy decreases by almost 24%, while that number is close to 60% for the weak-field case. This leads to increases of thermal energy, $E_t = p_g/(\gamma - 1)$, of about 3.3% (7.8%) in the strong-field (weak-field) case by the end of our simulation. Taking advantage of the symmetries and boundary properties in the simulations, it is straightforward to show that the mean thermal energy obeys the relation

$$\frac{\partial \langle E_t \rangle}{\partial t} = -\langle p_g \nabla \cdot u \rangle + \eta \langle j^2 \rangle + \left\langle \sigma_{ik} \frac{\partial u_i}{\partial x_k} \right\rangle , \quad (3.4)$$

where we have once again for heuristic purposes included effective resistive and viscous dissipation terms in addition to the consequences of adiabatic compression. Below we use equation (3.4) to estimate the degree to which our simulations are influenced by finite numerical resolution. In these calculations the total mass is conserved inside the grid. Furthermore, the use of periodic boundaries means that any adiabatic work applied to mass leaving the domain is exactly replaced by mass with identical properties entering from the opposite boundary; i.e., thermodynamically, the system is closed. Thus, since the average compression must be zero over the fixed volume, the net adiabatic work done on the gas is expected to be small, and the first term in equation (3.4) is small. Consequently, $\partial \langle E_t \rangle / \partial t$ must be due almost entirely to the two dissipative effects. We have verified numerically that $\langle p_g \nabla \cdot u \rangle$ is indeed small. There are no shocks formed in either of these cases, so only dissipation in

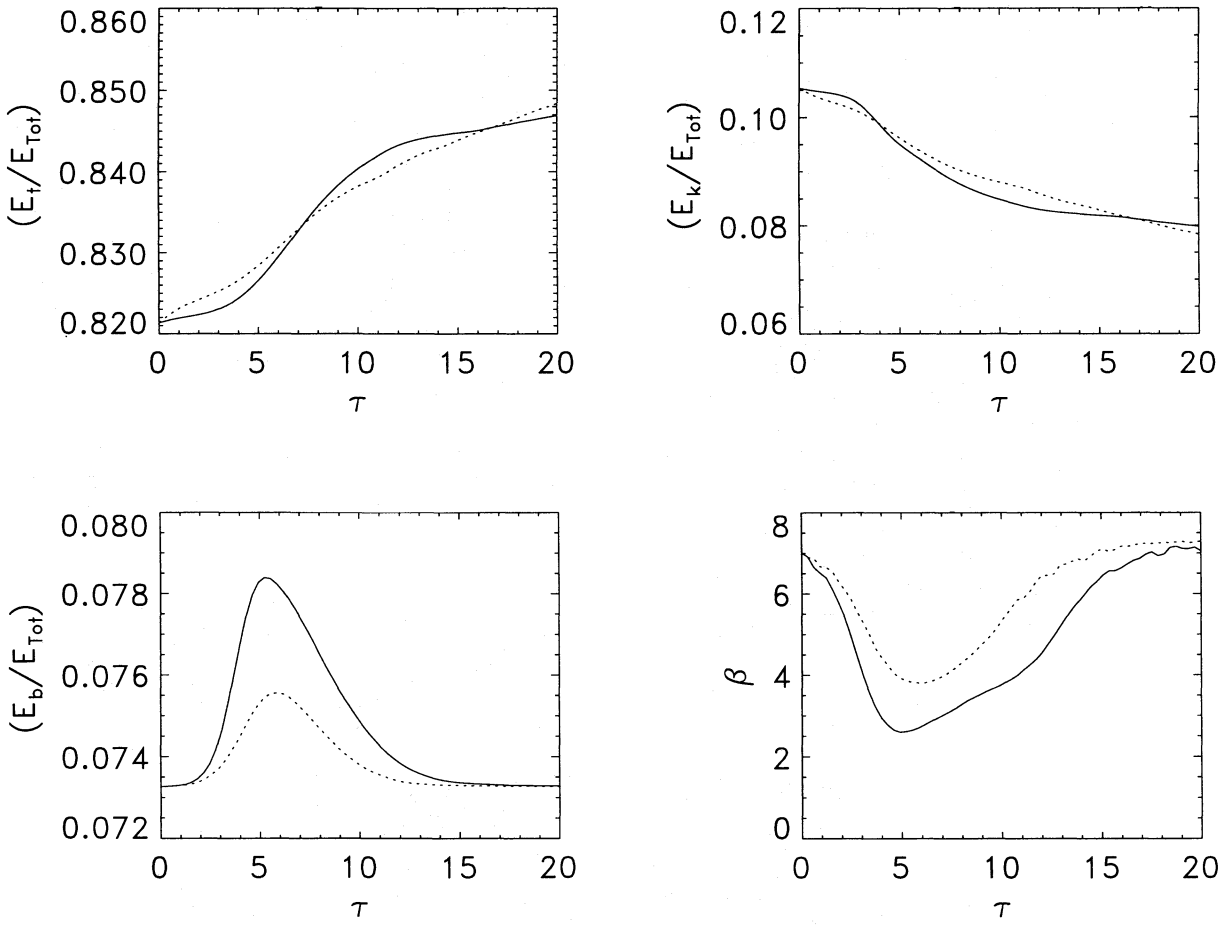

FIG. 7.—Evolution of energy components and β-parameter for the strong-field field case simulations. Shown are spatially averaged values of the thermal E_t (*upper left*), kinetic E_t (*upper right*), and magnetic energies E_b (normalized to the total energy $E_{Tot} = E_t + E_k + E_b$; *lower left*). In addition, we show the evolution of the minimum value on the computational grid of the plasma parameter $\beta = p_g/p_b$ (*lower right*). The solid, dotted, and dashed-dotted lines correspond to the high (512^2) and medium (256^2) resolution simulations, respectively.

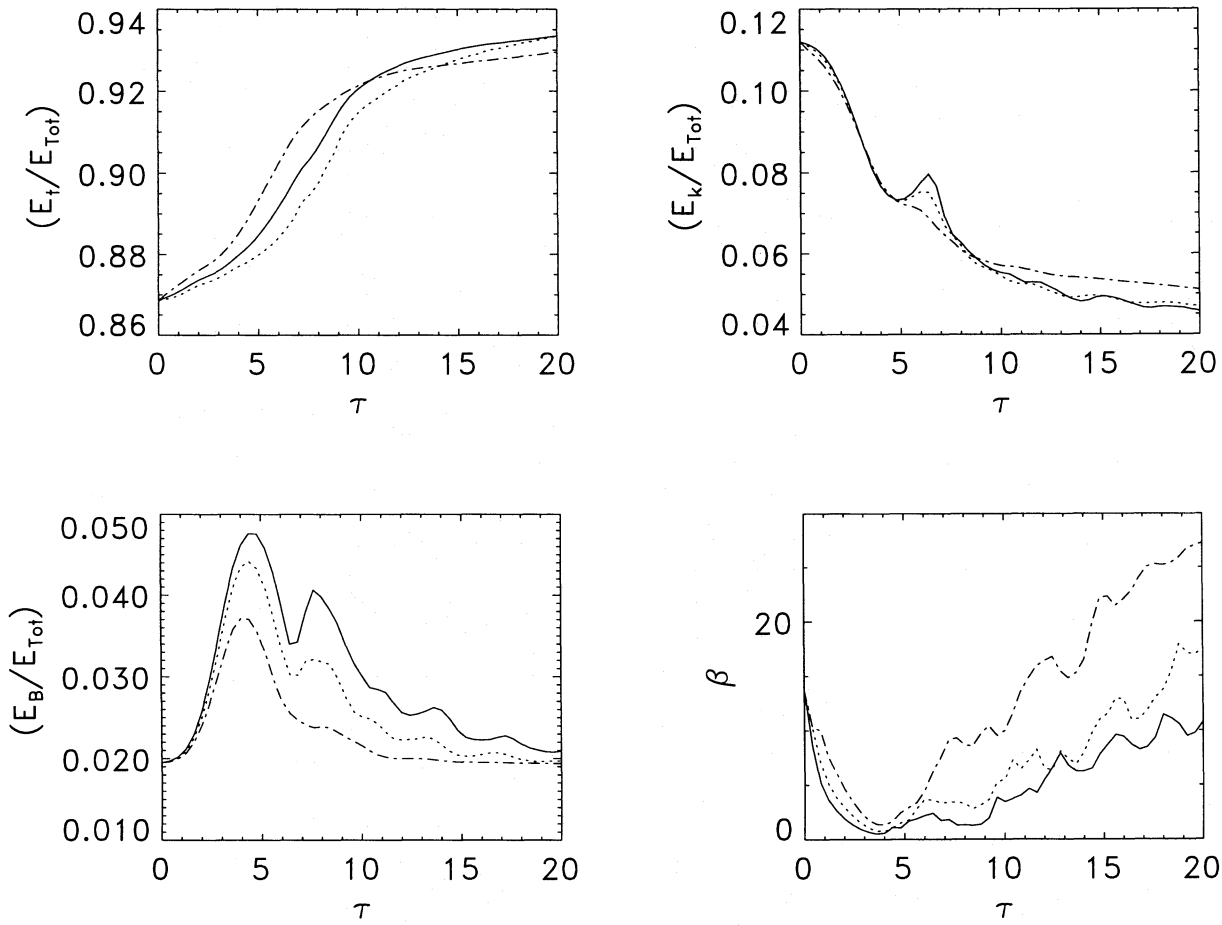

FIG. 8.—Same as Fig. 7 for the weak-field case simulations. The dashed-dotted lines correspond to the low-resolution simulation.

smooth flows matters. Even though the dissipation in our computation is numerical, that does not necessarily mean the simulated flows are physically incorrect, of course, at least in a statistical sense. Pseudo-ideal fluid simulations of shocks and turbulence, for example, depend on the existence of a small amount of numerical dissipation to obtain physically meaningful behaviors. But it is necessary that the numerical dissipation be small enough that the computed flows approach the intended physical flows (meaning those with very small viscosity and resistivity). To evaluate this situation we should ask how well the total dissipation in the simulated flows has converged. Examination of the time evolution of the thermal energies as shown in Figures 7 and 8 provides that information. The final increases in thermal energies agree among the different simulations of the same flows to within 10% of the same value in the strong-field case and about 6% for the weak-field case. Therefore, we consider the final states moderately well converged in that respect. We will explore in the next subsection some details about how that dissipation takes place prior to the development of the relaxed states.

We emphasize again that, although the final conditions of our simulations are not changing very fast, they cannot represent the expected conditions if one extended the computations for an arbitrarily long time. In fact, dissipation cannot entirely vanish so long as there is any shear left within the system. In the limit that the flow is laminar the viscous term in equation (3-4) can be represented qualitatively in terms of an effective shear viscosity, μ, and the mean-squared vorticity or enstrophy in the flow, $\langle W \rangle = \langle (\nabla \times u)^2 \rangle$, as $\langle \sigma_{ik}(\partial u_i/\partial x_k) \rangle \sim \mu \langle W \rangle$. From this and equation (3.4) the time for the flow kinetic energy to decay to thermal energy is more than Ra/U_o, where R is the effective viscous Reynolds number in the flow and a is the nominal width of the shear layer. Using the properties of our code as determined by Ryu et al. (1995) we can estimate that $R \gtrsim 10^5$ in our highest resolution runs. So, this decay time is several orders of magnitude longer than our simulation.

We noted earlier that the final magnetic field configuration in the weak-field case showed signs of an organized structure; namely flux tubes containing magnetic field lines aligned with the flow streamlines. The final state of the weak-field flow contains a second structure that warrants comment. Examination of Figures 3*a* and 4 shows, in addition, the presence of a low-density "channel" containing hot, high-entropy gas concentrated along the midplane. That feature does not correspond to the flux tubes, but rather lies between the flux tubes. The origin of this second feature becomes obvious if one views animations of the evolution of several quantities, especially the density, magnetic field, electric current, and entropy, $S = \ln(P/\rho^{5/3})$. Most of the entropy generated in dissipative events that we will describe in the next subsection has been concentrated into this thin layer, which appears to be contained by the two magnetic flux tubes, since they lie just outside it. Gas within the central layer is about 25% hotter than the average over the domain. The gas pressure is moderately

high within the layer, but there is a near equilibrium balance in the total pressure, $p + p_b$. Recalling that the flux tubes were traced to an early magnetic reconnection event separating the magnetic field in the outer and inner parts of the flow, we can recognize that a consequence of the evolution in the weak-field KH unstable flow has been a reorganization of the flow into two distinct regions; one in which the energy dissipation necessary for relaxation takes place and one that surrounds that region. There is no evidence of such a development in the strong-field flow, again presumably because the stronger initial field prevents the opportunity for the reorganization.

3.3. *Saturation and Relaxation*

As noted before, the history of a simulated two-dimensional ideal gasdynamic shear layer in a periodic flow is very simple; i.e., a single, long-lived vortex forms. That history seems quite distinct from what happens in the MHD flows, where the formation of vortices is either intermittent or entirely absent. In the weak-field case we computed the primary vortex begins development but is disrupted before it is fully formed. Its destruction leads to the generation of a sequence of smaller vortices (each located at one of the symmetry or node points in the computational plane), but they, too, are quickly destroyed. In the strong-field case the initial oscillation is stabilized before a vortex forms, and the flow then directly begins to approach a laminar shear layer. It might seem odd that our two MHD flows are so different, because their properties as given in Table 1 are the same except for a factor of 2 difference in the strength of the magnetic field. In both MHD flows the Alfvén Mach number is greater than unity and the plasma β parameter is substantially greater than one. However, it should be recalled that a parallel flow discontinuity is KH stable whenever the Alfvén Mach number $M_A < 2$, only slightly smaller than the value for our strong-field case. This criterion represents the condition that the restoring force from magnetic tension due to field line stretching along a perturbed boundary equals the "lift" force on the boundary. Thus, for our strong-field flow the initial Maxwell restoring force is only slightly less than needed to stabilize the oscillation. By comparing the magnitude of the Maxwell stress, $|(\boldsymbol{j} \times \boldsymbol{B})_y|$, and the gas pressure gradient, $|\partial p/\partial y|$, in the strong-field flow we confirmed directly that the initial perturbation grows only until the Maxwell stresses *along the displaced boundary* exceed the gas pressure gradient that drives the instability. From that moment, which is simultaneous with the peak in $\langle (u_y^2)^{1/2} \rangle$ in Fig. 1*a*, the two stresses seem quickly to achieve a close balance almost everywhere, while both transverse motions and excess magnetic energy steadily decay (see Figs. 1, 2, 3, and 7). Magnetic enhancements during the growth of the instability are concentrated into a close pair of magnetic flux tubes formed along the displaced flow boundary that have reduced plasma density and pressure. Although the total Maxwell stress does locally exceed the gas pressure gradient at saturation, the β parameter is never less than about 2.5 (see Fig. 7), so an "equipartition" in the common sense never develops. The total magnetic energy is enhanced by about 8% at its peak in the higher resolution simulation for this case. That compares to about a 9% enhancement reported for this case by Miura, so the agreement is reasonably good.

The early development of the weak-field flow is very different, of course, and resembles in most ways the behavior of the pure gasdynamical KH instability. Just as in the gasdynamic case the applied oscillation grows in amplitude and then begins to role up into a large vortex, as shown in Figure 3. However, it is well known that the presence of even an initially weak background magnetic field can have a profound influence on turbulent or sheared flows (see, e.g., Chandrasekhar 1960; Biskamp & Welter 1989; Cattaneo & Vainstein 1991; Balbus & Hawley 1991; Nordlund et al. 1992), especially if it has a nonvanishing mean vector value. That property is soon apparent in this simulation. Instead of rolling up and continuing to spin, the vortex formed in our weak-field flow becomes distorted in response to increases in magnetic field strength. Both magnetic pressure and tension contribute. That effect is apparent at $\tau = 5.6$ in Figure 3. The maximum total magnetic energy during the simulation occurs near this time. That energy, which exceeds the original value by $\sim 140\%$ in the highest resolution simulation of this case (see Fig. 8), is concentrated into a thin flux tube feature. Our peak magnetic energy enhancement in this simulation agrees well with that found by Malagoli et al. (1996) in their analogous calculation. The flux tube feature corresponds to the low-density plasma channel that approximately traces the displaced initial shear layer being wrapped into the vortex at this time. Miura pointed to the almost straight segment of that feature, centered on $x = L/4$ and called by him the "plasma depletion zone," as the place where most of the enhanced magnetic energy is concentrated. However, we find a much larger total magnetic energy enhancement (his was only 26%) and that by far the greater portion of the energy is held within the main vortex structure itself. In his computation, which had much lower resolution and, hence, greater diffusion and dissipation, the vortex was more strongly damped this time. We find, as well, a somewhat greater concentration of magnetic field within the plasma depletion zone, leading to a minimum $\beta = 0.55$, compared to the $\beta = 1.7$ that he quotes. We note that the plasma depletion zone seen at this time is *not* the same structure that leads to the two-dimensional flux tubes described for the final state. Those form separately and can be seen simultaneously with this feature at $\tau = 8$ in Figure 3*b*.

About the time, $\tau \approx 4.5$, that the magnetic energy is reaching its maximum, the total kinetic energy is at a local minimum (Fig. 8), a development also apparent in the first local minimum in $(\langle u_y^2 \rangle)^{1/2}$ seen in Fig. 1*b*. Thus, it is clear that magnetic stresses have impacted on the gasdynamics in a substantial way. Immediately after these developments, Figure 8 shows that the magnetic energy drops, while the kinetic energy rises. These further developments come from the fact that as the magnetic field is being drawn into the vortex, field lines from just outside the initial shear layer become folded back on themselves around the "tips" of the low-density channel (see Fig. 3*b*). The magnetic energy maximum corresponds to the moment just before the field becomes unstable to a tearing mode instability near the "tips." That leads to magnetic field reconnection and field annihilation. Blobs of heated, low-density plasma are ejected from the "tips" into the outer regions of the flow and the magnetic field reorganizes itself. The ejected blobs contain magnetic flux islands; i.e., closed flux loops. Within the vortex the field lines snap back toward the vortex center (accelerating plasma with them as they do so), while the exterior field structure becomes isolated from further involvement with vortex behaviors within the central shear

layer. The vortex collapses subsequently into the central shear layer.

As the original, primary vortex is destroyed in the manner just described, a strong, secondary vortex spins up, centered at $x = L/4$. That vortex also wraps and amplifies magnetic field within it, until at $\tau \approx 7.5$, field lines have been pulled completely around the outside of the vortex causing another reconnection event (see also Fig. 3). Once again, this event corresponds to a maximum in the total magnetic field energy. There is also a peak in the kinetic energy near this time, but this actually corresponds to the "ejection" of hot plasma from the primary vortex, at $\tau \approx 6$, when the magnetic energy is minimum. Magnetic energy and vorticity are concentrated around the perimeter of the vortex. That is also where reconnection begins. The reconnection event, as well as the one mentioned earlier, shows up clearly in images of such quantities as electric current, entropy, and β. Where magnetic "$\times$," or neutral, points form, intense local current sheets develop and excess entropy is generated, along with expansions in response to the heating. Local maxima in β also develop around the "$\times$" points, of course. As with the earlier vortex-directed magnetic reconnection, the initial reconnection event here separates magnetic field within and outside the vortex. In this case the magnetic field is somewhat weaker than before and the vortex is stronger. The vortex continues to spin for a while and the magnetic islands formed end up inside the vortex. It is a magnetically isolated structure, with detached fields lines surrounding it. The vortex and the magnetic energy within it decay by about $\tau \approx 10.5$. Remnant magnetic islands are still visible at $\tau = 10.4$ in Fig. 3*b*. Weaker vortices briefly form and decay at later times, leaving noticeable signature peaks in E_b around $\tau = 14$ and $\tau = 17$. Those features are anticorrelated with kinetic energy maxima at $\tau = 15$ and 18.

We commented earlier on the properties of the power spectrum of the magnetic pressure structure at the end of our simulations. To complete that discussion we briefly add a few comments about the power spectrum evolution during the saturation and relaxation phases for the weak-field case. There is little change in the P_x^b spectrum, except that as the secondary vortex strengthens it leads to a shift from dominance by the $k_x = 1$ mode to similar strength in both the $k_x = 1$ and $k_x = 2$ modes. For P_y^b the evolution is more remarkable in that power spikes at a number of scales are evident. The number and strength of those spikes changes as the number and scales of the dominant structures change. For example, as the primary vortex forms there is a single broad peak, around $k_y = 3$, which breaks up into at least four comparable narrow spikes at such wave modes as $k_y = 2$, 7, 9, and 13, once that physical feature is destroyed. Those are replaced during the life of the secondary vortex by a pair of comparable spikes at $k_y = 1$ and 7. The structure at $\tau = 14.4$ (see Fig. 3) leads to four comparable sharp power spectrum spikes at $k_y = 1$, 4, 6, and 9.

Since the secondary vortex is strong and spins several times before decay it presents a good opportunity to study the interactions of the flow and the magnetic field within it. The equation for the evolution of vorticity in two-dimensional ideal MHD can be written as

$$\frac{d\rho\omega}{dt} = [\nabla \times (\boldsymbol{B} \cdot \nabla)\boldsymbol{B}] + \nabla\rho \times \left(\frac{d\boldsymbol{u}}{dt}\right), \qquad (3.5)$$

with $\boldsymbol{\omega} = \nabla \times \boldsymbol{u}$. The $d\boldsymbol{u}/dt$ term in equation (3.5) represents the total acceleration of a fluid element due to all forces (see eq. [2.2]). For an entropic equation of state $\nabla\rho \times \nabla p = 0$, so the only nonvanishing contributions (for ideal flows) to the last term would come from the Lorentz force; i.e., $(1/\rho)\nabla\rho \times (\nabla \times \boldsymbol{B}) \times \boldsymbol{B}$. On the other hand, these flows are only slightly compressible ($M_s \sim 1$), so that $|1/\rho\nabla\rho| \ll 1$, and this term ought to be small. Then, with the aid of Stokes theorem we can relate the change in the total vorticity within an area to the line integral of the magnetic tension around the boundary

$$\int \frac{d(\rho\omega)}{dt} \cdot d\boldsymbol{A} \approx \oint (\boldsymbol{B} \cdot \nabla)\boldsymbol{B} \cdot d\boldsymbol{l} = \oint \boldsymbol{T} \cdot d\boldsymbol{l}\,. \qquad (3.6)$$

Figure 9 displays the two sides of equation (3.6) computed from the flow properties during the life of the secondary vortex, where the area integral was carried out over the vortex and the line integral surrounded it. The vorticity is positive inside the area, so the signs indicate a reduction in the strength of the vortex. Clearly the two quantities are in good agreement, so that equation (3.6) properly represents the evolution of the vortex. Magnetic tension around the vortex peaks in magnitude at $\tau = 7.5$, in agreement with the magnetic energy peak noted earlier. Between $\tau = 7$ and $\tau = 9.5$ the value of ρw_z inside the vortex decreases from its maximum value by about 75%. The integrated effect of magnetic tension according to equation (3.6) accounts for this change to within about 4%.

Finally, we make a few comments about the evolution of the cross helicity in the weak-field flow. The cross helicity, $\langle H \rangle$, (defined in eq. [3.1]) provides a way to express the self-organization of the flow. We already commented that at the end of our weak-field simulation the cross helicity approaches very close to its possible extrema, ± 1, in the bottom and top halves of the computational domain. The two signs just reflect differences in the initial velocity signs in the two regions of the grid. Since we began with a condition $\langle H \rangle = \pm 1$ in the appropriate halves, it may not be very surprising that the flows eventually return to that condition. In fact, if the flows were exactly laminar, this would necessarily be so. On the other hand, the flows still contain fluctuations at the end, and within those fluctuations the

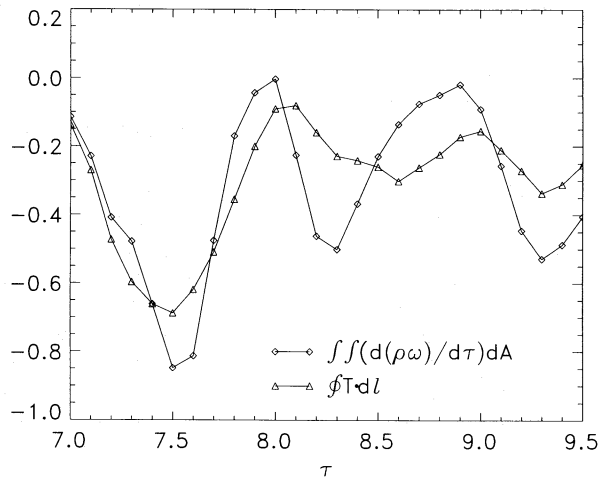

FIG. 9.—Evolution of the secondary vortex. Shown are the value of the surface integral of vorticity and line integral of magnetic tension in eq. (3.6). Note that the area integral was carried out over the vortex and the line integral surrounded it. The vorticity is positive inside the area, so the signs indicate a reduction in the strength of the vortex.

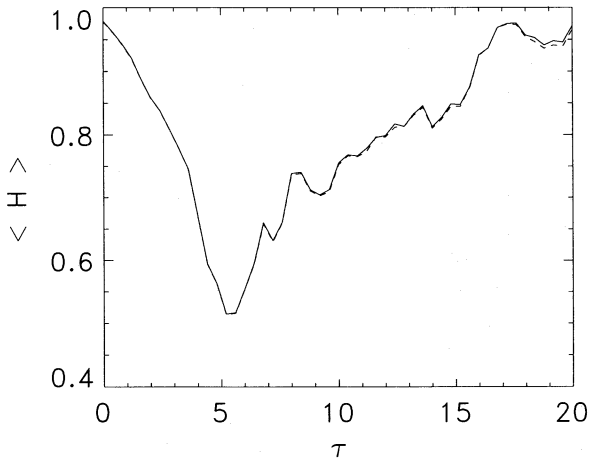

FIG. 10.—Evolution of the cross helicity for the high-resolution weak-field simulation. Shown are the values of $|\langle H \rangle|$, where $H = \int \hat{\boldsymbol{u}} \cdot \hat{\boldsymbol{B}}\, dx\, dy$. The dashed (dotted) line corresponds to the top (bottom) half-planes.

velocity and magnetic field structures are very well aligned. At intermediate times the cross helicity is only about half these extreme values, as can be seen in Figure 10. So, we believe this is an indication of real self-organization. Evidence for dynamical alignment can be found by comparing Figure 10 with Figure 6, which follows evolution of the mean squared magnetic field components. The initial large drop in $|\langle H \rangle|$ relates to the growth of the initial, primary vortex. We have already pointed out that the valleys in $\langle B_x^2 \rangle$ and $\langle B_y^2 \rangle$ correspond to reconnection events associated with various flow vortices. Each large increase in $|\langle H \rangle|$ visible in Figure 10 at, for example, $\tau = 7$, is generally simultaneous with one of those reconnection events, as well. Thus, the reconnection process serves to realign the flow and field vectors as the flow relaxes.

4. SUMMARY AND CONCLUSION

We have carried out numerical simulations of the evolution of unstable sheared MHD flows in two dimensions. Although we chose to conduct these experiments in a rather idealized setting, using a box that was periodic, we believe they have enabled us to discover several important insights about the nature of such flows that can be helpful in understanding more general situations. Our unperturbed initial conditions involved smooth shear layers of constant gas density separating flows with relative motions at sonic Mach number unity. There was a uniform magnetic field aligned with the flow.

We considered two cases. In the first the magnetic field strength was only slightly less than required to stabilize the perturbation. In the second case the magnetic field had a value 2.5 times smaller than that critical value. We followed each flow until it reached an apparently steady condition. For both flows the properties of that steady condition were fundamentally different from what happens in an analogous, two-dimensional gasdynamic unstable sheared flow. In the gasdynamic situation the flow evolves to include a single well-formed vortex that separates the two counterflowing fluids. That vortex would spin for a very long time, until viscous interactions spread it and dissipated it. By contrast, in the MHD flows, the steady condition that develops is one of a broad, nearly *laminar* layer separating the two counterflowing fluids. That difference is a consequence of the magnetic field aligned with the original shear layer. For the stronger magnetic field case this result is an obvious expectation, since magnetic tension stabilizes the instability before any vortices can develop and the flow relaxes in a straightforward manner to one that qualitatively resembles the initial conditions, except that the shear layer is broadened until it is stable against further perturbations. Because of the symmetries in our computations the mean vector magnetic field is a constant throughout each simulation, so the final magnetic field in this case is very little different from that at the beginning. The total magnetic energy, for example, is the same as at the start to within 1%. By the end of our simulation there is a rough equipartition between magnetic and kinetic energies, although both are small compared to the thermal energy contained within the gas.

That the quasi-steady, relaxed flow state should also be laminar for the weaker magnetic field is perhaps not so immediately obvious, since the initial magnetic energy is almost an order of magnitude less than the kinetic energy and more than an order of magnitude less than the thermal energy. It never becomes globally more than 5% of the total energy and never reaches global equipartition with the kinetic energy. What happens is that as vortices do develop within the flow, magnetic stresses are built up that have sufficient strength to locally modify the dynamics. At the same time a magnetic field wrapped into the vortices becomes unstable to tearing mode reconnection events that isolate some magnetic flux and lead to large-scale reorganization of other magnetic structures. The isolated magnetic flux is subsequently annihilated. Together these developments produce a reorganized flow and magnetic field in which the magnetic and flow fields are almost perfectly aligned. The magnetic field is also approximately as it was at the beginning in this case, except for a pair of stronger flux structures, or flux tubes, and fluctuations within them that appear to correspond to Alfvén waves propagating in the same direction as the fluid. However, close examination reveals that the magnetic energy is actually significantly greater than it was at the beginning. That difference comes through the formation the flux tubes. They formed out of an early magnetic reconnection episode that magnetically isolated the shear layer from adjacent plasma. Those flux tubes surround a sheet of hot, low-density gas that contains most of the excess entropy generated through the various reorganization events leading to relaxation. Thus, through the action of the magnetic field the flow has been reorganized into a thin, hot entropy layer surrounded by magnetically enhanced structures within a broad laminar shear layer. In this case the shear layer is much broader than for the stronger field case and actually substantially broader than the width of the single, "Cat's Eye," vortex that forms in the pure gasdynamic case. The last distinction results from the fact that magnetic reconnection following the initial generation of the vortex lead to a significant impulsive transfer of both energy and momentum away from the initial shear layer.

Even though our "weak-field" case had a magnetic field initially dynamically fairly small, it was strong enough that before the primary vortex could become fully developed, magnetic stresses became *locally* important. It is reasonable, therefore, to ask what differences should be expected when the initial field is initially truly very weak. Some discussions of MHD turbulence in this very weak-field regime (see, e.g.,

Ting et al. 1986) have argued that magnetic fields will never become dynamically important; i.e., the fields remain weak and passive. But, we suspect that the answer depends on the effective magnetic Reynolds of the flow, $R_m = U_o L/\eta$, comparing the rate at which magnetic field is rolled into a vortex to the rate at which it diffuses out of the vortex. The simulations in the Ting et al. (1986) study, for example, had modest magnetic Reynolds numbers, $R < 100$. On the other hand, as pointed out, for example, by Cattaneo & Vainstein (1991) and Cattaneo (1994), when the magnetic Reynolds number is big and there is a large-scale magnetic field, field line stretching can produce locally strong fields. In astrophysical flows we may often anticipate very large magnetic Reynolds numbers, so it is reasonable to expect in cases where the large-scale field starts out being quite small that it might eventually play a role in determining the outcome (This point has been made quite clearly with regard to MHD turbulent transport; Cattaneo & Vainstein 1991). As applied to the present problem, this would mean that the flows might exist longer as pseudo-gasdynamic, but that eventually field lines would be stretched sufficiently that magnetic tension would become locally involved in evolution of the vortex. This process should also, of course, naturally create tearing mode unstable magnetic topologies (see, e.g., Biskamp & Welter 1989), whose growth rates depend on the magnetic Reynolds number as well (see, e.g., Melrose 1986). That would provide a limiting process to accompany the eventual feedback on dynamical stresses. So, an outcome similar to what we have observed in the two cases studied here is still reasonable for very weak fields when the magnetic Reynolds number is large enough. In practical problems, where flow conditions may be more complex or time variable on large scales, these characteristics would have to be balanced against time and length constraints imposed by those features, of course.

This work by A. F., T. W. J., and J. B. G. was supported in part by the NSF through grants AST 91-00486 and AST 93-18959, by NASA through grant NAGW-2548 and by the University of Minnesota Supercomputer Institute. The work by D. R. was supported in part by the Basic Science Research Institute Program, Korean Ministry of Education 1994, Project no. BSRI-94-5408. We are grateful to Ibrahim Hallaj for very helpful assistance in analyzing the results. We also appreciate some very constructive comments on the manuscript by Akira Miura and Andrea Malagoli.

REFERENCES

Artola, M., & Majda, A. J. 1987, Physica D, 28, 253
Balbus, S., & Hawley, J. 1991, ApJ, 376, 214
Belle-Hamer, A. L., Fu, Z. F., & Lee, L. C. 1988, Geophys. Res. Lett., 15, 152
Belmont, G., & Chanteur, G. 1989, Phys. Scripta, 40, 124
Biskamp, D., & Welter, H. 1989, Phys. Fluids B, 1, 1964
Birkinshaw, M. 1991, in Beams and Jets in Astrophysics, ed. P. A. Hughes (Cambridge: Cambridge Univ. Press), 278
Blumen, W. 1970, J. Fluid Mech., 40, 769
Blumen, W., Drazin, P. G., & Billings, D. F. 1975, J. Fluid Mech., 71, 305
Cattaneo, F. 1994, ApJ, 434, 200
Cattaneo, F., & Vainstein, S. I. 1991, ApJ, 376, L21
Chandrasekhar, S. 1960, Proc. Nat. Acad. Sci., 46, 53
———. 1961, Hydrodynamic and Hydromagnetic Stability (New York: Oxford Univ. Press)
Corcos, G. M., & Sherman, F. S., 1984, J. Fluid Mech., 139, 29
Dobrowolny, M., Mangeney, A., & Veltri, P. 1980, Phys. Rev. Lett., 45, 144
Ferrari, A., Trussoni, E., & Zaninetti, L. 1981, MNRAS, 196, 1051
Fiedler, R. L., & Jones, T. W. 1984, ApJ, 283, 532
Landau, L. 1944, Akad. Nauk. S.S.S.R., Comptes Rendus (Doklady), 44, 139
Landau, L. D., & Lifshitz, E. M. 1987, Fluid Mechanics (Oxford: Pergamon)
Mac Low, M. M., McKee, C. F., Klein, R. I., Stone, J. M., & Norman, M. L. 1994, ApJ, 433, 757
Malagoli, A., Bodo, G., & Rosner, R. 1996, ApJ, 456, in press
Maslowe, S. A. 1981, in Hydrodynamic Instabilities and the Transition to Turbulence, ed. H. L. Swinney & J. P. Gollub (Berlin: Springer), 181
Melrose, D. B. 1986, Instabilities in Space and Laboratory Plasmas (Cambridge: Cambridge Univ. Press)
Miles, J. W. 1957, J. Acoust. Soc. Am., 29, 226
Miura, A. 1984, J. Geophys. Res., 89, 801
———. 1987, J. Geophys. Res., 92, 3195
———. 1990, Geophys. Res. Lett., 17, 749
———. 1992, J. Geophys. Res., 97, 10, 655
Miura, A., & Pritchett, P. L. 1982, J. Geophys. Res., 87, 7431 (MP)
Moffatt, H. K. 1978, Magnetic Field Generation in Electrically Conducting Fluids (Cambridge: Cambridge Univ. Press)
Nordlund, Å., et al. 1992, ApJ, 392, 647
Porter, D. H., & Woodward, P. R. 1994, ApJS, 93, 309
Pouquet, A 1978, J. Fluid Mech., 88, 1
Pouquet, A., Meneguzzi, M., & Frisch, U. 1986, Phys. Rev. A, 33, 4266
Priest, E. R. 1984, Solar Magnetohydrodynamics (Dordrecht: Reidel)
Ryu, D., & Jones, T. W. 1995, ApJ, 442, 228
Ryu, D., Jones, T. W., & Frank, A. 1995, ApJ, 452, 785
Tajima, T., & Leboeuf, J. N. 1980, Phys. Fluids, 23, 884
Ting, A. C., Matthaeus, W. H., & Montgomery, D. 1986, Phys. Fluids, 29, 3261
Wang, Y. M., & Robertson, J. A. 1984, A&A, 139, 103
Wu, C. C. 1986, J. Geophys. Res., 91, 3042
Zel'dovich, Ya. B. 1957, Soviet Phys.–JETP Lett., 4, 460